

grim: A Flexible, Conservative Scheme for Relativistic Fluid Theories

Mani Chandra

Department of Astronomy, University of Illinois, 1110 West Green Street, Urbana, IL, 61801; manic@illinois.edu

Francois Foucart

Lawrence Berkeley National Laboratory, 1 Cyclotron Rd, Berkeley, CA 94720, USA; Einstein Fellow; fvfoucart@lbl.gov

Charles F. Gammie

Department of Astronomy, University of Illinois, 1002 West Green Street, Urbana, IL, 61801

Department of Physics, University of Illinois, 1110 West Green Street, Urbana, IL, 61801; gammie@illinois.edu

ABSTRACT

Hot, diffuse, relativistic plasmas such as sub-Eddington black hole accretion flows are expected to be collisionless, yet are commonly modeled as a fluid using ideal general relativistic magnetohydrodynamics (GRMHD). Dissipative effects such as heat conduction and viscosity can be important in a collisionless plasma and will potentially alter the dynamics and radiative properties of the flow from that in ideal fluid models; we refer to models that include these processes as Extended GRMHD. Here we describe a new conservative code, **grim**¹, that enables all the above and additional physics to be efficiently incorporated. **grim** combines time evolution and primitive variable inversion needed for conservative schemes into a single step using an algorithm that only requires the residuals of the governing equations as inputs. This algorithm enables the code to be physics agnostic as well as flexibility regarding time-stepping schemes. **grim** runs on CPUs, as well as on GPUs, using the *same* code. We formulate a performance model, and use it to show that our implementation runs optimally on both architectures.

¹General Relativistic *Implicit* Magnetohydrodynamics: <http://github.com/afd-illinois/grim>. Commit hash used in this paper: 70bcd77

`grim` correctly captures classical GRMHD test problems as well as a new suite of linear and nonlinear test problems with anisotropic conduction and viscosity in special and general relativity. As tests and example applications, we resolve the shock substructure due to the presence of dissipation, and report on relativistic versions of the magneto-thermal instability and heat flux driven buoyancy instability, which arise due to anisotropic heat conduction, and of the firehose instability, which occurs due to anisotropic pressure (i.e. viscosity). Finally, we show an example integration of an accretion flow around a Kerr black hole, using Extended GRMHD.

1. Introduction

The fluid description of a plasma using the ideal general relativistic magnetohydrodynamic (GRMHD) equations is a workhorse in theoretical high energy astrophysics. The codes that solve these equations have been successfully applied in studies of various processes of interest such as jet formation and accretion onto compact objects. Many important results have emerged from numerical solutions of the ideal GRMHD equations. A few examples are the validation that the Blandford & Znajek 1977 mechanism occurs naturally in a global MHD model (McKinney & Gammie 2004), the discovery of magnetically choked accretion flows (McKinney et al. 2012; Tchekhovskoy et al. 2011), and simulated observations of Sgr A* (Mościbrodzka et al. 2009).

However, the ideal GRMHD model is readily justified only when the Knudsen number $Kn = l_{mfp}/l_{system} \ll 1$, where l_{mfp} is the mean free path, and l_{system} is the characteristic length scale of the system, and when the ratio of the time scales $\tau_C/\tau_D \ll 1$, where τ_C is the two-body Coulomb scattering time scale, and τ_D is the dynamical time scale in the system. In other words, the ideal GRMHD model assumes that the plasma is locally in equilibrium. This leads to a simple set of conservation laws for mass and momentum and all that is required to complete the system is a prescription for the pressure, which is usually approximated by a Gamma-law equation of state. While this simplicity is appealing, systems such as low luminosity black holes which accrete through a radiatively inefficient accretion flow (RIAF) are in the $Kn \gg 1$ regime.

In a RIAF, the synchrotron cooling time scales are much longer than the dynamical time scale. This leads to the accreting plasma becoming virially hot as the gravitational potential energy is stored as internal energy, with $T \sim R^{-1}$, where T is the temperature of the plasma, and R is the radius from the black hole. The disk is then geometrically thick, and optically thin (Yuan & Narayan (2014)) and the Coulomb mean free paths between all

the constituent particles (ion-ion, ion-electron, electron-electron) (all of which scale as $\sim T^2$) are much larger than the typical system scale GM/c^2 (Mahadevan & Quataert 1997). Thus, it is not evident that ideal GRMHD is applicable.

Despite the divergence of the Knudsen number, and the collisional time scale, there are indeed small parameters that can be exploited to recover an effective hydrodynamic description. In the presence of a sufficiently strong magnetic field, the following conditions can apply: $l_{gyro}/l_{system} \ll 1$, and $t_{gyro}/t_{system} \ll 1$, where l_{gyro} is the gyroradius and t_{gyro} is the gyroperiod. These apply in most astrophysical systems. For example, in Sgr A*, Faraday rotation measurements and observed synchrotron radiation indicate a magnetic field strength ~ 100 Gauss and number density $\sim 10^7 \text{ cm}^{-3}$. implying $l_{gyro}/l_{system} \sim 10^{-5}$ and $t_{gyro}/t_{system} \sim 10^{-8}$. Thus, particles are constrained to move along field lines. In the presence of weak collisionality, perhaps provided by wave-particle scattering, this leads to set of fluid-like equations with anisotropic transport along the magnetic field lines.

Dissipative relativistic fluid theories should be hyperbolic, causal, and stable. Early theories by Eckart 1940 and Landau-Lifshitz do not satisfy these requirements whereas these are conditionally satisfied by the Israel & Stewart 1979 theory of dissipative hydrodynamics (Hiscock & Lindblom 1983, 1985, 1988,b). Chandra et al. 2015 adapted the Israel & Stewart 1979 theory for isotropic conduction and viscosity, taking into account the symmetries imposed on the distribution function of a plasma in the presence of a magnetic field to derive a one-fluid model of a plasma that incorporates anisotropic thermal conduction and viscosity. The conduction is driven by temperature gradients along field lines and the viscosity due to a shear flow projected onto the field lines. The model, referred to as extended magnetohydrodynamics (EMHD), is valid up to second order deviations from equilibrium and is applicable to weakly collisional flows. We review the equations of the model in section (§4) and encourage the interested reader to look at Chandra et al. 2015 for the derivation and the limits of the model within which it satisfies the above mentioned constraints. In this paper, we derive a variety of analytic and semi-analytic solutions, described in (§8), to develop intuition about the EMHD model, and to serve in a test suite for the numerical implementation of EMHD and similar models.

The methods used to integrate the equations of relativistic MHD are similar to those used in non-relativistic MHD, namely, shock capturing conservative schemes using the finite volume method. In particular, the approximate Riemann solvers used to compute the numerical fluxes at cell interfaces, and the various methods available to evolve the magnetic field under the constraint $\nabla \cdot \mathbf{B} = 0$ are similar for relativistic and non-relativistic MHD. One of the main complication in relativistic MHD is the mathematical relation between the evolved variables and physical variables. Consider special-relativistic ideal hydrodynamics,

where the physical variables to be solved for, referred to as *primitive variables*, are the rest mass energy density ρ , the internal energy u and the spatial components of the four-velocity u^i . The variables are evolved using the continuity equation $\partial_\mu(\rho u^\mu) = 0$, and the energy and momentum conservation equations given by $\partial_\mu T^{\mu\nu} = 0$, where $T^{\mu\nu} = (\rho + u + P)u^\mu u^\nu + P\eta^{\mu\nu}$ is the perfect fluid stress tensor, m is the particle mass, $\eta^{\mu\nu} = \text{diag}(-1, 1, 1, 1)$ is the flat space metric, and P is the pressure, approximated here by a gamma-law equation of state, $P_g = (\gamma - 1)u$. Conservative schemes time-step the *conserved variables*, $\mathbf{U} = (\rho u^0, T^{0\nu})$, from \mathbf{U}^n to \mathbf{U}^{n+1} , where the superscripts $n, n + 1$ indicate the discretized time levels. To recover the primitive variables ρ^{n+1} , u^{n+1} and $(u^i)^{n+1}$ at the new time step from \mathbf{U}^{n+1} requires the solution to a set of nonlinear equations and is a multivariate nonlinear root finding problem (although for hydrodynamics it can be reduced to a univariate nonlinear problem). This is unlike non-relativistic fluid dynamics, where this recovery step is algebraic.

Many schemes have been proposed for the recovery of primitive variables from conserved variables in relativistic hydrodynamics (Noble et al. 2006). However, the introduction of new physics, as in the EMHD model, voids the earlier algorithms, which are specialized to ideal MHD. The model has equations governing the dissipative quantities q , the heat flux along the magnetic field lines, and ΔP , the pressure anisotropy, which are of the form $\partial_t q \sim \hat{b}^\mu \partial_\mu T + \hat{b}^\mu u^\nu \partial_\nu u_\mu$ and $\partial_t \Delta P \sim \hat{b}^\mu \hat{b}^\nu \partial_\mu u_\nu$, where T is the temperature and \hat{b}^μ is the unit vector along the direction of the magnetic field. The difficulty is that the equations for q and ΔP are sourced by *spatio-temporal* derivatives and not just spatial derivatives. The values of q^{n+1} and ΔP^{n+1} depend on the values of T^{n+1} and u_ν^{n+1} , but these in turn need to be recovered from the conserved quantities \mathbf{U}^{n+1} . Now, the stress-tensor has dissipative contributions of the form $T^{\mu\nu} \sim q(\hat{b}^\mu u^\nu + \hat{b}^\nu u^\mu) + \Delta P \hat{b}^\mu \hat{b}^\nu$ and so \mathbf{U}^{n+1} itself depends on q^{n+1} and ΔP^{n+1} . Thus, the time evolution of all thermodynamic quantities are nonlinearly intertwined with primitive variable recovery.

grim recasts the entire time stepping procedure as a coupled multivariate nonlinear root finding problem. Consider as a simple example the following system of 1D wave-equations:

$$\partial_t u_1 + c \partial_x u_1 = 0 \tag{1}$$

$$\partial_t u_2 + c \partial_x u_2 = 0 \tag{2}$$

for the variables $u_1(x, t)$ and $u_2(x, t)$. Now, performing an explicit first order spatio-temporal discretization, we have $(u_{1,2}^{i,n+1} - u_{1,2}^{i,n})/\Delta t + c(u_{1,2}^{i+1,n} - u_{1,2}^{i,n})/\Delta x = 0$ (assuming $c > 0$), where the index i denotes a grid zone and the index n denotes a time level. Here, both $u_1^{i,n+1}$ and $u_2^{i,n+1}$ can be solved for algebraically, $u_{1,2}^{i,n+1} = u_{1,2}^{i,n} - c\Delta t/\Delta x(u_{1,2}^{i+1,n} - u_{1,2}^{i,n})$. In **grim**, we find instead the values of $u_1^{i,n+1}$ and $u_2^{i,n+1}$ that satisfy

$$\mathbf{f}(u_1^{i,n+1}, u_2^{i,n+1}) \equiv \left\{ \begin{array}{l} (u_1^{i,n+1} - u_1^{i,n})/\Delta t + c(u_1^{i+1,n} - u_1^{i,n})/\Delta x \\ (u_2^{i,n+1} - u_2^{i,n})/\Delta t + c(u_2^{i+1,n} - u_2^{i,n})/\Delta x \end{array} \right\} = 0, \tag{3}$$

where $\mathbf{f}(u_1^{i,n+1}, u_2^{i,n+1})$ are the *residuals*, and represent the governing equations in their discretized form. This system of equations (which in general are nonlinearly coupled) is now solved using an iterative algorithm until $|\mathbf{f}(u_1^{i,n+1}, u_2^{i,n+1})| < \epsilon$, where $|\cdot|$ is a suitable norm and ϵ is a chosen tolerance. The algorithm requires as sole input the residuals $\mathbf{f}(\dots)$, which are the discretized form of the governing equations. The algorithm is independent of the physics that constitutes the discretized equations $\mathbf{f}(\dots)$ and is therefore independent of the underlying physical model. It works with ideal MHD, EMHD, and possible extensions of the EMHD model. Thus, the abstraction of numerical solution to a set of PDEs as a non-linear root finding problem allows for flexibility regarding the governing equations, as well as time-stepping schemes as we shall show in later sections.

We begin in §2 by describing the numerical discretization of a set of hyperbolic PDEs to $O(\Delta x^2, \Delta t^2)$ using the finite volume method combined with a semi-implicit time stepping scheme. We then proceed in §3 to recast the time stepping of the discrete system as a non-linear multivariate root finding problem and describe how the roots are obtained using a residual-based algorithm. We then apply this technique to the EMHD model in §4, along with a review of the governing equations. We detail the implementation of all the above in §5, and describe the techniques, and libraries we use that enable us to use either CPUs, or GPUs. We then report various performance and scaling data in §6. In order to understand the performance numbers, we formulate a performance model in §7, and use it to show that our implementation is optimal on both CPUs, and GPUs. We have developed an extensive test suite for the EMHD model which we present in §8, and validate `grim` using this test suite, thus demonstrating its utility in exploring the solution space of this model. In §9, we show example applications of `grim`; buoyancy instabilities that occur in weakly collisional plasmas, and accretion onto supermassive black holes. Finally, in §§10, we conclude.

2. Finite volume method

`grim` uses the finite volume method to solve hyperbolic partial differential equations in their conservative form

$$\partial_t U + \partial_j F^j = S \tag{4}$$

where U is the vector of *conserved* quantities, F^j are *fluxes*, and S are *sources*. We break down the full scheme into (§2.1) domain discretization, (§2.2) integral form of the differential equations, (§2.3) time stepping scheme, and (§2.4) spatial discretization.

2.1. Grid Generation

We are primarily interested in solving (4) in simple rectangular and spherical geometries. To discretize these domains, we work in coordinates where the boundaries of the domains are aligned with the coordinate axes. For example, Cartesian coordinates $x^i = \{x, y, z\}$ for rectangular domains, and spherical polar coordinates $x^i = \{r, \theta, \phi\}$ for spherical geometries. Then, given the extent of the domain in these coordinates $[x_{start}^i, x_{end}^i]$, a grid with $N_1 \times N_2 \times N_3$ zones is generated by decomposing the spatial domain into zones with dimensions $dx^1 \times dx^2 \times dx^3$, where $dx^i = (x_{end}^i - x_{start}^i)/N^i$, for $i = 1, 2, 3$. This results in a uniform mesh in each coordinate.

If a physical problem requires concentration of grid zones in a specific region, we construct a smooth curvilinear non-uniform grid using a coordinate transformation, as is done in the `harm` code (Gammie et al. 2003). First, a uniform grid is generated in a different set of coordinates X^i , and then transformed to the x^i coordinates using $x^i \equiv x^i(X^j)$. The grid zones in X^i all have equal dimensions $dX^1 \times dX^2 \times dX^3$, where $dX^i = (X_{end}^i - X_{start}^i)/N^i$, and $[X_{start}^i, X_{end}^i]$ is the extent of the domain in the new coordinates. This corresponds to a grid spacing $dx^i = L_j^i dX^j$ in x^i , where $L_j^i \equiv \partial x^i / \partial X^j$ is the transformation matrix. Depending on the form of $x^i(X^j)$, a non-uniform grid is generated in the x^i coordinates.

Below, we illustrate the grid generation for a domain enclosed by two spherical shells. We concentrate the grid zones near the inner radius r_{in} using a $\log(r)$ grid, and near the midplane $\theta = \pi/2$, with an adjustable parameter $h = (0, 1]$. As $h \rightarrow 0$, there is greater concentration of the zones near the midplane.

$$x^1 \equiv r = \exp(X^1) \tag{5}$$

$$x^2 \equiv \theta = \pi X^2 + \left(\frac{1-h}{2}\right) \sin(2\pi X^2) \tag{6}$$

$$x^3 \equiv \phi = X^3 \tag{7}$$

$$L_j^i = \begin{pmatrix} \exp(X^1) & 0 & 0 \\ 0 & \pi(1 + (1-h)\cos(2\pi X^2)) & 0 \\ 0 & 0 & 1 \end{pmatrix} \tag{8}$$

The boundaries of the domain in $x^i = \{r, \theta, \phi\}$ are $[r_{in}, r_{out}] \times [0, \pi] \times [0, 2\pi]$, which correspond to $[\log(r_{in}), \log(r_{out})] \times [0, 1] \times [0, 1]$ in $X^i = \{X^1, X^2, X^3\}$ coordinates.

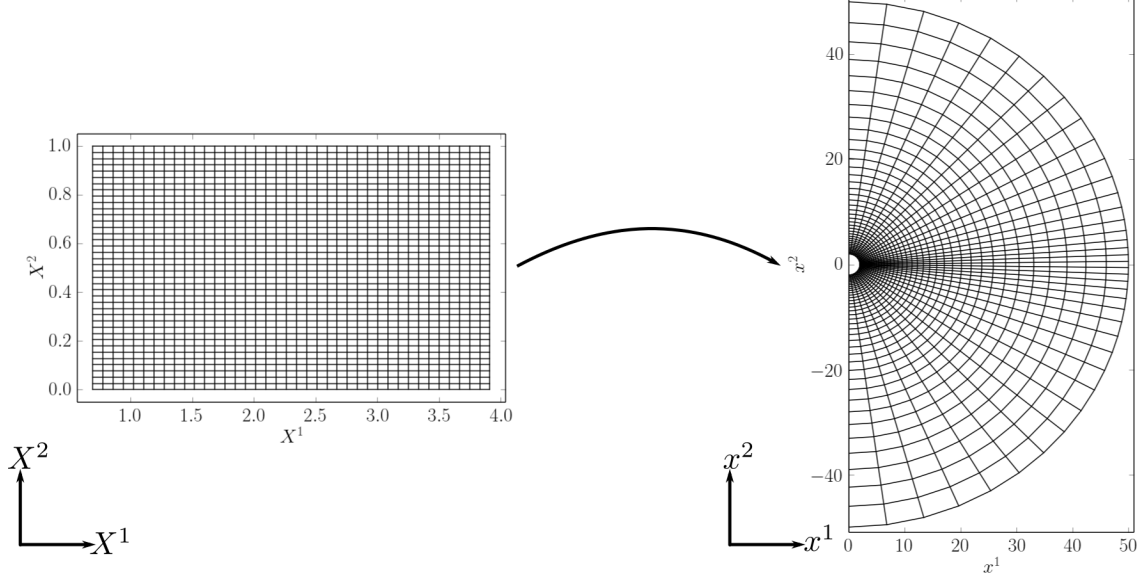


Fig. 1.— Generation of a spherical grid with mid-plane grid refinement, with the refinement parameter $h = 0.3$ in (6). The left side shows the grid in the computational coordinates (X^1, X^2) that `grim` works in, and the right side shows the grid in Cartesian coordinates.

2.2. Integral Form of the Differential Equations

We now setup the finite volume formulation in the (X^1, X^2, X^3) coordinate system. Multiplying (4) by the area of the *control volume* (see fig) $\Delta v = dX^1 dX^2 dX^3$, we get

$$\partial_t \int U \Delta v + \int dX^1 \partial_1 \left(\int F^1 dX^2 dX^3 \right) + \int dX^2 \partial_2 \left(\int F^2 dX^1 dX^3 \right) + \dots = \int S \Delta v \quad (9)$$

Rewriting the above in terms of *cell-averages* $\bar{U} \equiv \int U \Delta v / \int \Delta v$, $\bar{S} \equiv \int S \Delta v / \int \Delta v$ and the *face-averages* $\bar{F}^1 \equiv \int F^1 dX^2 dX^3 / \int dX^2 dX^3$, $\bar{F}^2 \equiv \int F^2 dX^1 dX^3 / \int dX^1 dX^3$, and $\bar{F}^3 \equiv \int F^3 dX^1 dX^2 / \int dX^1 dX^2$

$$\partial_t \bar{U} + \frac{\bar{F}^1_{\text{right}} - \bar{F}^1_{\text{left}}}{\Delta X^1} + \frac{\bar{F}^2_{\text{top}} - \bar{F}^2_{\text{bottom}}}{\Delta X^2} + \frac{\bar{F}^3_{\text{front}} - \bar{F}^3_{\text{back}}}{\Delta X^3} = \bar{S} \quad (10)$$

where we have replaced $\int dX^1 \partial_1()$ in (9) by the surface integral of F^1 on the *right* and *left* surfaces of the control volume (see fig. 2.4.2), and $\int dX^2 \partial_2()$, $\int dX^3 \partial_3()$ have been replaced by surface integrals of F^2 on the *top* and *bottom* surfaces, and similarly for F^3 on the *front* and *back* surfaces respectively. The above equations (10) are an *exact* integral reformulation of the differential equations (4) over the control volume. Multiplying (10) by

$\int dt$ and performing the integration over a discrete time interval Δt ,

$$\bar{U}_{n+1} - \bar{U}_n + \frac{\int dt \bar{F}_{\text{right}}^1 - \int dt \bar{F}_{\text{left}}^1}{\Delta X^1} + \frac{\int dt \bar{F}_{\text{top}}^2 - \int dt \bar{F}_{\text{bottom}}^2}{\Delta X^2} + \dots = \int dt \bar{S} \quad (11)$$

where the index n indicates the discrete time level. Equations (11) are evolution equations for the zone-averaged conserved variables \bar{U}_{n+1} , which are in turn (non-linear) functions of the zone-averaged primitive variables \bar{P}_{n+1} , i.e., $\bar{U}_{n+1} \equiv U(\bar{P}_{n+1})$.

To proceed, we need to evaluate the spatial integrals $\int dv$ and the temporal integrals $\int dt$ in (11) using a numerical quadrature to a desired order. We opt for a *truncation error* of $O(\Delta t^2, \Delta X_i^2)$. The required accuracy can be achieved by evaluating the spatial integrals as $\int dX^1(\cdot) \rightarrow \Delta X^1(\cdot)_i$, $\int dX^2(\cdot) \rightarrow \Delta X^2(\cdot)_j$, and $\int dX^3(\cdot) \rightarrow \Delta X^3(\cdot)_k$ where the spatial integer indices i , j , and k indicate the zone centers in the X^1 , X^2 and X^3 directions respectively. The outcome of this quadrature procedure is that the cell-averaged conserved variables \bar{U} , and the cell-averaged source terms \bar{S} can be replaced by point values $U_{i,j,k}$ and $S_{i,j,k}$ at the center of a grid zone and the face-averaged fluxes \bar{F}^1 in the X^1 direction can be replaced by point values at the centers of the *right* and *left* faces, $\bar{F}_{\text{right}}^1 \approx F_{i+1/2,j,k}^1$ and $\bar{F}_{\text{left}}^1 \approx F_{i-1/2,j,k}^1$ respectively. The substitution for the face-averaged fluxes \bar{F}^2 in the X^2 direction, and \bar{F}^3 in the X^3 direction, by point values follows on similar lines.

2.3. Time stepping scheme

The temporal integral $\int dt(\cdot)$ for the various terms in (11) is approximated to $O(\Delta t^2)$ using a two-stage *semi-implicit* scheme designed to deal with stiff source terms. Depending on the theory being solved for, the source terms can have spatio-temporal derivatives $S \equiv S(P, \partial_t P, \partial_i P)^2$. We separate these as $S = S^I(P) + S^E(P) + A^t(P)\partial_t P + A^i(P)\partial_i P$, where $S^{I,E}(P)$ denote source terms to be treated implicitly (I) or explicitly (E), and $A^t(P)$, $A^i(P)$ are the coefficients of the temporal $\partial_t P$ and spatial derivative terms $\partial_i P$ respectively. The spatial derivative terms, when present in the sources, are evaluated using slope limited derivatives on a symmetric stencil (currently the generalized minmod slope using a 3 points stencil, although higher-order schemes inspired by the WENO5 (Liu et al. 1994; Jiang & Shu 1996) and PPM (Colella & Woodward 1984) methods are also implemented). The scheme proceeds in two stages:

- First, we take a *half step* to go from $P_n \rightarrow P_{n+1/2}$, where the index $n + 1/2$ indicates

²This is an unconventional definition of source terms, but it allows us to use a notation that is as closely analogous to non-relativistic fluids as possible.

the half time step. The temporal integrals for the fluxes $\partial_i F^i$, for the explicit sources S^E , and for the spatial derivative terms in the sources are evaluated explicitly using $\int dt(\cdot) \rightarrow (\Delta t/2)(\cdot)_n$, whereas the sources S^I are treated implicitly using $\int dt(\cdot) \rightarrow (\Delta t/2)((\cdot)_{n+1/2} + (\cdot)_n)$. This leads to the following discrete form

$$\begin{aligned} \frac{U(P_{n+1/2}) - U(P_n)}{\Delta t/2} + \frac{F_{right}^1(P_n) - F_{left}^1(P_n)}{\Delta X^1} + \dots = \frac{1}{2} (S^I(P_{n+1/2}) + S^I(P_n)) \quad (12) \\ + S^E(P_n) + A^t(P_n) \frac{P_{n+1/2} - P_n}{\Delta t/2} + A^i(P_n) \partial_i P_n \end{aligned}$$

- Next, we take a *full step* from $P_n \rightarrow P_{n+1}$. The temporal integrals for $\partial_i F^i$, S^E , and $A^i(P) \partial_i P$ are evaluated using $\int dt(\cdot) \rightarrow \Delta t(\cdot)_{n+1/2} + O(\Delta t^2)$. This is performed using $P_{n+1/2}$ obtained from the half step. The source terms S^I are treated implicitly using $\int dt(\cdot) \rightarrow \Delta t((\cdot)_{n+1} + (\cdot)_n) + O(\Delta t^2)$

$$\begin{aligned} \frac{U(P_{n+1}) - U(P_n)}{\Delta t} + \frac{F_{right}^1(P_{n+1/2}) - F_{left}^1(P_{n+1/2})}{\Delta X^1} + \dots = \frac{1}{2} (S^I(P_{n+1}) + S^I(P_n)) \quad (13) \\ + S^E(P_{n+1/2}) + A^t(P_{n+1/2}) \frac{P_{n+1} - P_n}{\Delta t} \\ + A^i(P_{n+1/2}) \partial_i P_{n+1/2} \end{aligned}$$

where (...) denote flux discretizations in X^2 , and X^3 , which we have not written for brevity.

The separation between explicit and implicit sources $S^{I,E}$ is problem-dependent. Stiff source terms are treated implicitly, while computationally expensive source terms can be treated explicitly if desired. For additional flexibility, nonlinear source terms can also use a mixed implicit-explicit approach. For example, the extended MHD algorithm has source terms of the form

$$S(P) = \frac{P - P_0(\partial_i P)}{\tau_R[P]} \quad (14)$$

where τ_R is a potentially small damping timescale. In this case, it is advantageous to treat $P/\tau_R[P]$ implicitly and P_0 explicitly. But it is also preferable to use a consistent damping timescale $\tau_R[P]$ for all terms. Accordingly, for the half time step we use

$$\int dt S(P) = \frac{\Delta t}{2} \left(\frac{P_{n+1/2} + P_n}{2\tau_R[P_n]} - \frac{P_0(\partial_i P_n)}{\tau_R[P_n]} \right), \quad (15)$$

and for the full time step,

$$\int dt S(P) = \Delta t \left(\frac{P_{n+1} + P_n}{2\tau_R[P_{n+1/2}]} - \frac{P_0(\partial_i P_{n+1/2})}{\tau_R[P_{n+1/2}]} \right). \quad (16)$$

This is easily implemented as long as the implicit source terms S^I have access to P_n during the half step and $P_{n+1/2}$ during the full step. In practice, for any system of equations, the user is responsible for providing functions $S^I(P, P^E)$, $S^E(P^E), \dots$, with $P^E = P_n$ for the half-step and $P^E = P_{n+1/2}$ for the full step. The code then assembles the evolution equations from the discretization described in this section.

Evidently, the above system of equations obtained using a semi-implicit temporal discretization requires us to solve a set of non-linearly coupled equations for $P_{n+1/2}$ and P_{n+1} in the half step (12), and the full step (13) respectively. Further, the presence of time derivatives $A^t(P)\partial_t P$ in the source terms implies that we cannot separately time step the conserved variables $U_n \rightarrow U_{n+1} \equiv U(P_{n+1})$, and invert them later to obtain P_{n+1} , as is usually the case. The time stepping and the inversion must be done simultaneously. We describe the algorithm to do this in (§3). However, we note that equations without implicitly coupled source terms are treated explicitly, and do not require the nonlinear solver.

2.4. Flux Computation

The computation of the face-centered fluxes $F_{i-1/2}^1 \equiv F_i^1(P_{i-1/2}^-, P_{i-1/2}^+)$, and $F_{i+1/2}^1 \equiv F_{i+1/2}^1(P_{i+1/2}^-, P_{i+1/2}^+)$ requires two stages: (1) *reconstruction* of the primitive variables from the cell centers $P_{\dots, i-1, i, i+1, \dots}$ to the left $P_{i-1/2, i+1/2}^-$, and right $P_{i-1/2, i+1/2}^+$ side of the face centers at $i - 1/2, i + 1/2$, and (2) a *Riemann solver* to evaluates the fluxes $F_{i-1/2, i+1/2}^1$ given the left $P_{i-1/2, i+1/2}^-$ and the right states $P_{i-1/2, i+1/2}^+$.

2.4.1. Reconstruction

The face-centered primitive variables are obtained using a reconstruction operator R . The operator takes as input the values of adjacent zone-centered primitive variables to construct a polynomial interpolant to a desired order inside the zone, which is then evaluated at the face-centers. We now describe the reconstruction procedure in one dimension, along X^1 . For brevity, we suppress the X^2 and X^3 zone indices. Multi-dimensional reconstruction proceeds by performing the one-dimensional reconstruction separately in each direction.

For a zone with center i , the reconstruction operator R is used in two ways depending on the input order. In the case of a 3-point reconstruction stencil, we use $R_i^+ = R(P_{i-1}, P_i, P_{i+1})$ to give $P_{i+1/2}^-$, the primitives variables on the left side of the *right* face of the zone and $R_i^- = R(P_{i+1}, P_i, P_{i-1})$ to give $P_{i-1/2}^+$, the primitive variables at the right side of the *left* face of the zone. This procedure is repeated for the zone with center $i - 1$ with R_{i-1}^+ to obtain

$P_{i-1/2}^-$, and for the zone with center $i+1$ with R_{i+1}^- to obtain $P_{i+1/2}^+$. We now have the states $P_{i-1/2}^{-,+}$ needed by the Riemann solver to compute the fluxes $F_{i-1/2} \equiv F_{i-1/2}(P_{i-1/2}^-, P_{i-1/2}^+)$, and $P_{i+1/2}^{\pm}$ needed to compute $F_{i+1/2} \equiv F_{i+1/2}(P_{i+1/2}^-, P_{i+1/2}^+)$.

2.4.2. Riemann Solver

For generic systems of equations, we have to rely on relatively simple Riemann solvers – at least if we want to avoid numerical computation of the characteristic speeds and eigenvectors of the evolution system. Here, we rely on either the Local Lax Friedrich (LLF) flux, or the HLLE flux (Harten et al. 1983). The LLF and HLLE solvers rely on the knowledge of the fluxes F_i^{\pm} and the conservative variables U_i^{\pm} on the right/left side of face i . Both are computed directly from the reconstructed primitive variables P_i^{\pm} . For the LLF flux, we also use an estimate of the maximum characteristic speed on face i , $c_{\max,i} \geq \max(|c_{j,i}^{\pm}|)$, where $c_{j,i}$ is the j^{th} speed on face i . The LLF flux is then

$$F_i^{\text{LLF}} = \frac{F_i^+ + F_i^-}{2} - \frac{c_{\max,i}}{2}(U_i^+ - U_i^-). \quad (17)$$

Similarly, the HLLE flux relies on estimates of the maximum left-going and right-going characteristic speeds on face i , $c_{\max,i}^R \geq \max(c_{j,i}^+, 0)$ and $c_{\max,i}^L \geq \max(-c_{j,i}^-, 0)$. The HLLE flux is then

$$F_i^{\text{HLLE}} = \frac{c_{\max,i}^R F_i^- + c_{\max,i}^L F_i^+ - c_{\max,i}^R c_{\max,i}^L (U_i^+ - U_i^-)}{c_{\max,i}^L + c_{\max,i}^R}. \quad (18)$$

The HLLE flux is generally less dissipative than the LLF flux in regimes where $v^i \gtrsim c_{\max}$. The two are identical when the maximum left-going and right-going speeds are equal, but the HLLE flux smoothly switches to upwind reconstruction when all characteristic speeds have the same sign (e.g., for ideal hydrodynamics, when the speed of the flow across face i is supersonic). In practice, as the computation of the characteristic speeds for the ideal MHD and EMHD systems can be costly, we replace c_{\max}^R and c_{\max}^L with simpler analytic upper bounds appropriate for the evolved system of equations.

3. General Root Finder

The spatio-temporal discretization of (4) leads to nonlinear equations (12) for $P_{n+1/2}$ and (13) for P_{n+1} . We solve these using an iterative Newton algorithm with a numerical Jacobian assembly, and a backtracking linesearch. The only input to the root finder is a residual function. Thus, we begin by recasting the equations to be solved for, as residuals

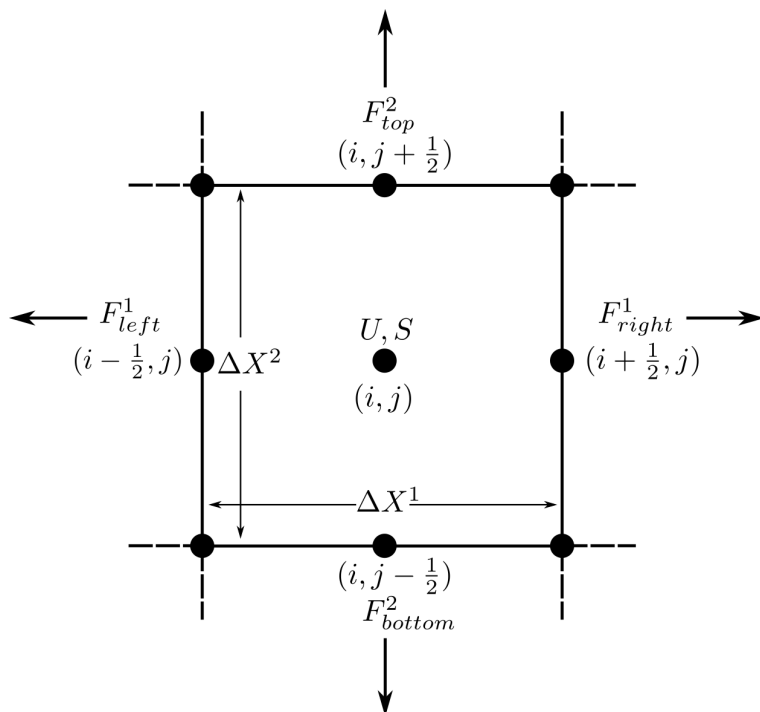


Fig. 2.— Schematic of a grid zone in 2D. In 3D, there are two additional faces along X_3 , which we denote by *front* and *back*.

$R(P)$, where R is the vector of equations, and P are the unknown primitive variables. For example, the residuals for the half step evolution (12) are

$$R(P_{n+1/2}) = \frac{U(P_{n+1/2}) - U(P_n)}{\Delta t/2} + \frac{F_{right}^1(P_n) - F_{left}^1(P_n)}{\Delta X^1} + \dots \quad (19)$$

$$- S^E(P_n) - \frac{1}{2} (S^I(P_{n+1/2}) + S^I(P_n)) - A^t(P_n) \frac{P_{n+1/2} - P_n}{\Delta t/2} - A^i(P_n) \partial_i P_n$$

Given the residuals as a function of the unknowns $R \equiv R(P)$, the algorithm proceeds by starting with a guess for the unknowns $P_{n+1/2}$ and iterating using

$$P^{k+1} = P^k + \lambda^k \delta P^k \quad (20)$$

for $k = 0, 1, \dots, k_{max}$ till $\|R(P)\| < tol$, where $\|\cdot\|$ is a suitable norm, tol is a desired tolerance, δP^k is a linear correction which we describe in (§3.1), and $\lambda^k \in (0, 1]$ is a *linesearch* parameter, which is determined by a quadratic backtracking linesearch strategy that we describe in (§3.2). In writing the above, we have suppressed the half step index $n + 1/2$.

3.1. Residual-based Jacobian Computation

The correction δP^k at each nonlinear iteration k is obtained by solving the following linear system of equations

$$\mathbf{J}(P^k) \delta P^k = -R(P^k) \quad (21)$$

where the matrix $\mathbf{J}(P^k)$ is the $N_{var} \times N_{var}$ Jacobian of the system evaluated at P^k , and N_{var} is the number of primitive variables being solved for. The Jacobian itself is assembled numerically from the residual function $R(P)$ to $O(\epsilon)$, where ϵ is a small differencing parameter. Column i , and row j of the numerical Jacobian are computed using

$$\mathbf{J}_{i,j}(P^k) \approx \frac{R_i(P_{\epsilon}^k) - R_i(P^k)}{P_{j,\epsilon}^k - P_j^k}, \quad (22)$$

and the perturbed unknowns P_{ϵ}^k are given by

$$P_{\epsilon}^k = (1 + \epsilon)P^k(1 - \text{small}(P^k)) + \epsilon * \text{small}(P^k) \quad (23)$$

where

$$\text{small}(P^k) = \begin{cases} 1, & |P^k| < 5\epsilon \\ 0, & \text{otherwise} \end{cases}$$

The use of the function $\text{small}(P^k)$ in P_{ϵ}^k prevents a division by zero in (21). In the absence of $\text{small}(P^k)$, this occurs when any component of $P^k = 0$, leading to $P_{\epsilon}^k = 0$.

3.2. Line Search

The traditional Newton algorithm is given by (20), with $\lambda^k = 1$. This is however not robust, and can diverge from the solution. When that happens we *backtrack* by choosing $\lambda \in (0, 1]$ according to the following strategy:

- Initialize $\lambda^k = 1$.
- If $\|R(P^k + \lambda^k \delta P^k)\| < \|R(P^k)\|(1 - \epsilon_{BT} \lambda^k)$, accept the new guess $P^{k+1} = P^k + \lambda^k \delta P^k$ for the primitive variables and exit the linesearch. Otherwise, continue to the computation of a new λ^k . In **grim**, we set the small parameter $\epsilon_{BT} = 10^{-4}$. If this condition is satisfied, we know that the current guess $P^k + \lambda^k \delta P^k$ provides at least some improvement over the previous guess P^k .
- Find the new linesearch parameter λ_{new} by minimizing the function

$$f(\lambda^k) = \|R(P^k + \lambda^k \delta P^k)\|^2, \quad (24)$$

modeling f as a quadratic function of λ and using the fact that $df/d\lambda[\lambda = 0] = -2f(0)$ (as δP^k is the solution of the linear problem at P^k). We then have

$$\lambda_{\text{new}}^k = \frac{f(0)}{f(\lambda_{\text{old}}^k) + (2\lambda_{\text{old}}^k - 1)f(0)} \lambda_{\text{old}}^2. \quad (25)$$

We then set $\lambda^k = \lambda_{\text{new}}^k$, and go back to the previous step.

We note that this procedure is performed separately at each point.

4. Extended GRMHD

The EMHD model (Chandra et al. 2015) is a one-fluid model of a plasma consisting of electrons and ions. It considers the following number current vector N^μ for the ions (set to be the same for electrons) and total (electrons+ions) stress-tensor $T^{\mu\nu}$

$$N^\mu = nu^\mu \quad (26)$$

$$T^{\mu\nu} = (\rho + u + \frac{1}{2}b^2)u^\mu u^\nu + (P_g + \frac{1}{2}b^2)h^{\mu\nu} - b^\mu b^\nu + q^\mu u^\nu + q^\nu u^\mu + \Pi^{\mu\nu} \quad (27)$$

where n is the number density of ions, which is equal to the number density of electrons, $\rho = (m_i + m_e)n \approx m_i n$ is the total rest mass energy density, m_e and m_i are the electron and proton

rest masses, u is the total internal energy, P is the total pressure approximated by a Gamma-law equation of state $P_g = (\gamma - 1)u$, u^μ is a four-velocity whose choice here corresponds to an observer comoving with the number current, also known as the Eckart frame, and b^μ is a magnetic field four-vector whose components are given by $b^t = B^i u^\mu g_{i\mu}$, $b^i = (B^i + b^t u^i)/u^t$, where the magnetic field 3-vector $B^i = F^{*it}$, and F^{*} is the dual of the electromagnetic field tensor. The tensor $h^{\mu\nu}$ is the projection operator onto the spatial slice orthogonal to u^μ , $h^{\mu\nu} = g^{\mu\nu} + u^\mu u^\nu$. The four-vector q^μ is a heat flux and the tensor $\Pi^{\mu\nu}$ models viscous transport of momentum. The model ignores bulk viscosity and resistivity. The equations governing ρ , u , and u^μ are given by the usual conservation equations,

$$\nabla_\mu N^\mu = 0 \quad (28)$$

$$\nabla_\mu T_\nu^\mu = 0 \quad (29)$$

Expanding the covariant derivative ∇_μ in a coordinate basis,

$$\partial_t (\sqrt{-g} \rho u^t) + \partial_i (\sqrt{-g} \rho u^i) = 0 \quad (30)$$

$$\partial_t (\sqrt{-g} T_\nu^t) + \partial_i (\sqrt{-g} T_\nu^i) = \sqrt{-g} T_\lambda^\kappa \Gamma_{\nu\kappa}^\lambda \quad (31)$$

where (30) has been obtained from (28) by scaling with m_i . The equations governing the components of the magnetic field 3-vector B^i are given by the induction equation in the ideal MHD limit

$$\partial_t (\sqrt{-g} B^i) + \partial_j (\sqrt{-g} (b^j u^i - b^i u^j)) = 0. \quad (32)$$

The heat flux q^μ and the shear stress $\Pi^{\mu\nu}$ that appear in the total stress tensor (27) are

$$q^\mu = q \hat{b}^\mu \quad (33)$$

$$\Pi^{\mu\nu} = -\Delta P \left(\hat{b}^\mu \hat{b}^\nu - \frac{1}{3} h^{\mu\nu} \right). \quad (34)$$

where the scalar q is the magnitude of the heat flux that flows parallel to the magnetic field lines and the scalar $\Delta P = P_\perp - P_\parallel$ is the pressure anisotropy i.e., the difference in pressures perpendicular P_\perp and parallel P_\parallel to the magnetic field. The above forms of the heat flux q^μ and the shear stress $\Pi^{\mu\nu}$ have been derived by assuming that the distribution functions of all species are gyrotropic, which is accurate in the limit that the Larmor radii are much smaller than the system scale. The evolution of q and ΔP are given by

$$\frac{dq}{d\tau} = -\frac{q - q_0}{\tau_R} - \frac{q}{2} \frac{d}{d\tau} \log \left(\frac{\tau_R}{\chi P^2} \right) \quad (35)$$

$$\frac{d\Delta P}{d\tau} = -\frac{\Delta P - \Delta P_0}{\tau_R} - \frac{\Delta P}{2} \frac{d}{d\tau} \log \left(\frac{\tau_R}{\rho \nu P} \right), \quad (36)$$

where $d/d\tau = u^\mu \nabla_\mu$ and

$$q_0 \equiv -\rho \chi \hat{b}^\mu (\nabla_\mu \Theta + \Theta a_\mu) \quad (37)$$

$$\Delta P_0 \equiv 3\rho\nu(\hat{b}^\mu \hat{b}^\nu \nabla_\mu u_\nu - \frac{1}{3} \cdot \nabla_\mu u^\mu) \quad (38)$$

Here, $\Theta = P/\rho \equiv kT/m_i c^2$ is the ion temperature, $a^\mu \equiv u^\nu \nabla_\nu u^\mu = u^\nu \partial_\nu u^\mu + \Gamma_{\nu\kappa}^\mu u^\nu u^\kappa$ is the four-acceleration and χ, ν are the ion thermal and viscous diffusion coefficients respectively. The equations for the heat flux q and the pressure anisotropy ΔP are obtained by enforcing the second law of thermodynamics. The result then is that q and ΔP relax to q_0 and ΔP_0 over the time scale τ_R , with the additional term in (35) and (36) being of a higher order (if $q \sim \epsilon \ll 1$, then, $qd(\log(\tau_R/(\chi P^2)))/d\tau \sim \epsilon^2$ and similarly for ΔP). The terms q_0 (37) and ΔP_0 (38) which q and ΔP relax to respectively, are covariant generalizations of the Braginskii (1965) closure, which the model reduces to in the limit where the relaxation time scale $\tau_R \rightarrow 0$. The above equations (35) and (36) can be rescaled and written

$$\nabla_\mu(\tilde{q}u^\mu) = -\frac{\tilde{q} - \tilde{q}_0}{\tau_R} + \frac{\tilde{q}}{2} \nabla_\mu u^\mu, \quad (39)$$

$$\nabla_\mu(\Delta\tilde{P}u^\mu) = -\frac{\Delta\tilde{P} - \Delta\tilde{P}_0}{\tau_R} + \frac{\Delta\tilde{P}}{2} \nabla_\mu u^\mu, \quad (40)$$

with

$$\tilde{q} = q \left(\frac{\tau_R}{\chi\rho\Theta^2} \right)^{1/2} \quad (41)$$

$$\Delta\tilde{P} = \Delta P \left(\frac{\tau_R}{\nu\rho\Theta} \right)^{1/2}. \quad (42)$$

These rescaled equations are crucial to our numerical implementation. Equations (35) and (36) have higher order terms $q/2 d(\log(\tau_R/(\chi P^2)))/d\tau$ and $\Delta P/2 d(\log(\tau_R/(\rho\nu P)))/d\tau$ which we find are numerically difficult to handle in low density regions. If these terms are ignored, the positivity of entropy production is no longer guaranteed. However, the rescaled equations (39), and (40) do include these terms, and using these equations guarantees adherence to the second law of thermodynamics (up to truncation error in the numerical solution), as well as leads to well behaved numerical solutions.

To conclude, the model evolves, (1) the ion rest mass density ρ , (2) the total internal energy density u , (3) the spatial components u^i of the four-velocity u^μ , (4) the components of the magnetic field three-vector B^i , (5) the ion heat flux along magnetic field lines q and (6) the ion pressure anisotropy ΔP , for a total of ten variables. The governing equations are the continuity equation (30) for ρ , the energy and momentum conservation equations (31) for u

and u^i respectively, the induction equation (32) for B^i , and the relaxation equations (39), and (40) for q and ΔP respectively. The inputs to the model are the transport coefficients χ , the thermal diffusivity, and ν , the kinematic viscosity. A closure scheme for χ and ν as a function of the relaxation time scale τ_R is described in Chandra et al. (2015). The scheme accounts for the presence of kinetic plasma instabilities at subgrid scales, which are prevalent in weakly collisional/collisionless plasmas. In that closure, we set $\chi = \phi c_s^2 \tau_R$ and $\nu = \psi c_s^2 \tau_R$, where ϕ , and ψ are non-dimensional numbers ~ 1 , c_s is the sound speed, and the damping timescale τ_R models the effective collision timescale for ions due to kinetic plasma instabilities.

4.1. Wave Speeds

The approximate Riemann solvers allowing us to capture shocks in `grim` require at least an upper bound on the characteristic speeds (See §2.4.2). The speeds control the amount of numerical dissipation introduced in the evolution. To minimize numerical dissipation, the speed estimates should be as close as possible to the true characteristic speeds, but for stability the estimates should be an upper bound on the true speeds. In ideal hydrodynamics, the characteristic speeds of the system are known analytically, but this is no longer the case for even ideal MHD. The characteristic speeds of our EMHD model can be found numerically, but this requires finding the largest and smallest zeroes of a 10^{th} degree polynomial on both sides of every cell face. To avoid this expensive operation, we instead follow the methods often implemented in the ideal MHD simulations which use the HLLC or LLF Riemann solvers, and consider an upper bound on the maximum wave speed in the fluid frame, v_{\max} . We can then obtain upper bounds on the maximum right-going and left-going wave speeds by computing the grid-frame velocity of waves propagating at $\pm v_{\max}$ in the rest frame of the fluid, in the direction along which the flux is being computed. A more detailed discussion of the wave speeds of the EMHD model is provided in Chandra et al. (2015). Here we will only note that we use the practical upper bound

$$v_{\max}^2 = \tilde{c}_s^2 + v_A^2 - \tilde{c}_s^2 v_A^2 \quad (43)$$

where v_A is the usual Alfvén speed and \tilde{c}_s is a correction to the sound speed including the effects of heat conduction and viscosity:

$$v_A^2 = \frac{b^2}{\rho + \gamma u + b^2} \quad (44)$$

$$c_s^2 = \frac{\gamma(\gamma - 1)u}{\rho + \gamma u} \quad (45)$$

$$\tilde{c}_s^2 = \frac{1}{2} \left(c_s^2 + v_q^2 + \sqrt{c_s^4 + v_q^4} \right) + v_{\Delta P}^2. \quad (46)$$

The corrections v_q and $v_{\Delta P}$ to the sound speed c_s are

$$v_q^2 = (\gamma - 1) \frac{\chi}{\tau_R}, \quad (47)$$

$$v_{\Delta P}^2 = \frac{4\nu}{3\tau_R}. \quad (48)$$

With the closure scheme in (Chandra et al. 2015), the speed \tilde{c}_s simplifies to

$$\tilde{c}_s^2 = \frac{c_s^2}{2} \left(1 + (\gamma - 1)\phi + \sqrt{(1 + (\gamma - 1)^2\phi^2 + \frac{8\psi}{3}} \right). \quad (49)$$

From this equation and the inequality $c_s^2 \leq (\gamma - 1)$, we can also derive conditions on ψ and ϕ which guarantee $v_{\max}^2 < 1$. This is a sufficient, but not necessary, condition for the system to be causal and hyperbolic. For $\psi = \phi$ and the standard choice of $\gamma = 4/3$ (resp. $5/3$), we find $\psi_{\max} \approx 1.3$ (resp. $\psi_{\max} \approx 0.29$). As, at the level of the Riemann solver, we do not assume a specific closure scheme in `grim`, we implement Eq. 46 for \tilde{c}_s , and not the simplified version.

4.2. Constrained Transport

A crucial ingredient for the evolution of the induction equation (32) is the preservation of the zero monopole constraint $\nabla \cdot \mathbf{B} = 0$. Naive evolution leads to uncontrolled growth of the constraint, resulting in numerical instabilities. Constrained transport schemes (Evans & Hawley 1988) exactly preserve a specific numerical representation of the constraint, i.e., the violations are at machine tolerance.

We use a version of constrained transport by Tóth 2000, the *flux-CT* scheme, where the magnetic fields are co-located with the fluid variables, at the cell-centers³. They then

³We are currently testing a version that uses face centered formulation.

are evolved by the same routines in a finite volume sense, with the “fluxes” being the electric fields (up to a sign), which for the EMHD model (just as in ideal MHD) are $F^j = \sqrt{-g} (b^j u^i - b^i u^j)$. At the end of the update the face centered fluxes F_{face}^j (i.e. the electric fields) obtained from the Riemann solver are averaged to the edges to get the edge centered fluxes F_{edge}^j . The edge centered fluxes are then averaged to get new face centered fluxes \bar{F}_{face}^j , which are then used to evolve the volume averaged magnetic fields $\int B^i \Delta v$. The simple averaging procedure we use $F_{\text{face}}^i \rightarrow F_{\text{edge}}^i$ is the original Tóth 2000 formulation, which is also being used in the `harm` code, and lacks upwinding information (see Gardiner & Stone 2005 for a discussion on the limitations of this approach).

5. Implementation Details

We now discuss the implementation of the algorithms described in the previous sections. `grim` is written in C++, with a modular library architecture. Different components such as spatial reconstruction, the Riemann solver, boundary conditions, and evaluation of the metric and related quantities are all separate libraries. Each library has automated unit tests to ensure robustness against inadvertent programmer errors ⁴.

`grim` is designed to run on existing, as well as upcoming architectures. It has been tested and benchmarked on CPUs as well as on Nvidia and AMD GPUs. In (§7), we formulate a performance model, and describe the specifications of a machine that `grim` is most sensitive to. Guided by the model, we have optimized `grim` to achieve a significant fraction of machine peak on both CPU and GPU systems.

5.1. Dependencies

`grim` is built on top of the PETSc (Balay et al. 2016) library to handle distributed memory parallelism, and the ArrayFire (Yalamanchili et al. 2015) library for shared memory parallelism within a node. The C++ vector abstractions from ArrayFire allow `grim` to run on a variety of computer architectures (CPUs and GPUs) using the *same* code. We discuss this in detail in (§5.2) and then describe how we integrate PETSc and ArrayFire to achieve architecture agnostic distributed memory parallelism in (§5.3).

⁴At present, 75 units tests.

5.2. Architecture Agnostic Code

There are now several supercomputers ⁵ that, in addition to CPUs, have accelerators such as GPUs. The programming models for these two architectures are different. We are able to write a single code that runs on both architectures by performing operations within a node using the `array` data structure from the `ArrayFire` library. Operations to be performed on an `array` are written down in a vector notation. For example, to add `array A`, `array B`, and write to `array C`, each of which hold multidimensional data, we write `C = A + B` to perform the operation over the entire domain. At runtime, `ArrayFire` detects the available compute architectures on the node, and fires kernels customized to that architecture, using either an `OpenCL`, `CUDA`, or `CPU` backend.

The use of vector notation also significantly simplifies the code. The entirety of our implementation of the nonlinear solver §3, including the Jacobian assembly §3.1, the linear inversion (21), and the quadratic backtracking linesearch §3.2 is 250 lines (including comments).

All the mathematical operations that need to be performed in `grim` can be divided into two categories, *local* operations that operate point-wise, and *non-local* operations that require data from adjacent grid zones, such as reconstruction. We describe how both of these are implemented using the vector notation.

5.2.1. Local Operations

A majority of calculations in `grim` such as computing the conserved variables $U(P)$, the fluxes $F^{1,2,3}(P)$, and the various source terms $S^{I,E}(P)$, $S(\partial_t P)$ involve point-wise operations. These are easily implemented in vector notation, with certain caveats. As will be described in (§7), the speed of vector-vector operations is set completely by the available memory bandwidth of the system, and therefore it is crucial to maximize the *effective* bandwidth.

We illustrate what effective bandwidth means with the following computation: we have a contravariant four-vector u^μ , that we want to transform to a covariant four-vector u_μ , using $u_\mu = g_{\mu\nu}u^\nu$, where $g_{\mu\nu}$ is the metric. Converting to computer code in vector notation, we have

```
for (int mu=0; mu < 4; mu++)
{
```

⁵www.top500.org


```

uCov[mu] = 0;
for (int nu=0; nu < 4; nu++)
{
    uCov[mu] += gCov[mu][nu]*uCon[nu];
}
}

```

Each of `uCov[mu]`, `uCov[mu]`, `gCov[mu][nu]`, `uCon[nu]` is an array of size $N_1 \times N_2 \times N_3$, where N_1 , N_2 , and N_3 are the number of grid zones in the X^1 , X^2 , and X^3 directions respectively, on each node. The operation `uCov[mu] += gCov[mu][nu]*uCon[nu]`, occurs over all $N_1 \times N_2 \times N_3$ grid zones.

Notice that `uCon[nu]`, `nu = 0, 1, 2, 3`, is being read for the computation for each of `uCov[mu]`, `mu = 0, 1, 2, 3`. For grid sizes that exceed the cache, as is the case with production science runs, this involves reads from slow global memory and is therefore a performance bottleneck. In this case, the computation of `uCov[mu]` involves 32 global reads (16 for `gCov[mu][nu]`, and $4 \times 4 = 16$ for `uCon[nu]`). An optimal implementation would involve 20 global reads, with only 4 reads for `uCon[nu]`. Therefore, the effective bandwidth achieved is only $20/32 \approx 0.62$ of the ideal value. Thus, while the abstraction of mathematical operations using vector notation allows for computation to be performed on a wide variety of computer architectures, further innovation is required to ensure optimality of the computation.

The feature that enables near-optimal performance of point-wise vector computations is `ArrayFire`'s *lazy* evaluation using its Just-In-Time (JIT) compiler. To avoid multiple reads of the memory, the operations that need to be performed on the arrays `uCov[mu]` are queued, instead of being immediately executed (known as *eager* evaluation, as is usually the case). Execution occurs using `eval(uCov[0], uCov[1], uCov[2], uCov[3])`. The JIT analyses the common dependencies between all four arrays, and fires a single kernel without any redundant reads and writes. In the above example, this leads to a single read for `uCon[mu]` instead of four separate reads. Our measurements indicate that this leads to architecture independent optimal effective bandwidth, which is crucial to the performance of our nonlinear solver. We discuss this further in (§7).

5.2.2. Non-local Operations

Operations such as reconstruction and interpolation can be thought of as non-local operations because they operate on stencils of non-zero width, as opposed to point-wise local operations that operate on stencils of zero width. Non-local operations are performed

using discrete convolutions. The abstraction of finite differences as discrete convolutions has two advantages: (1) it allows for architecture agnostic code since all we require is an optimized convolution routine for CPUs and GPUs, and (2) there are indeed optimized convolution routines for both these architectures because convolutions are crucial to image processing.

A discrete convolution of input data g , with a filter f , at a point $n \in [0, N)$ is defined as

$$(f * g)[n] \equiv \sum_{m=-M}^M f[m]g[n - m] \quad (50)$$

where g is an `array` of size N , and the filter f has a stencil width $2M + 1$ with extent $\{-M, -M + 1, \dots, 0, \dots, M - 1, M\}$. Forward differences $dg_+[n] \equiv g[n + 1] - g[n]$ are computed using $f = \{1, -1, 0\}$, while backward differences $dg_-[n] \equiv g[n] - g[n - 1]$ are computed using $f = \{0, 1, -1\}$. Central differences $dg \equiv g[n + 1] - g[n - 1]$ are simply $dg = dg_+ + dg_-$.

We use the optimized `convolve()` function provided by `ArrayFire` that takes in an input `array g` of size N , and a set of P filters $\mathbf{f}_1, \mathbf{f}_2, \dots, \mathbf{f}_P$, and simultaneously operates all filters over the input data to return an `array h` with dimensions $N \times P$. The `array h` then contains the forward dg_+ , and backward differences dg_- along a specified direction, over the entire domain. The combination of these two with vectorized conditional operators such as `c = min(a, b)` allows us to implement the slope limiters that are required for the reconstruction operation.

5.3. Parallelization Infrastructure

One of the many mundane tasks involved in writing a finite volume code is the allocation of memory and initialization of several $N_1 \times N_2 \times N_3 \times N_{var}$ arrays, where N_1 , N_2 , and N_3 are the number of grid zones along X^1 , X^2 and X^3 directions respectively, and N_{var} is the number of variables at each grid zone.

In addition to the memory allocation, there are several other functions the code needs for (1) partitioning the data across several nodes in a distributed memory cluster, (2) communication of ghost zones between nodes that share the same boundary, and (3) parallel file input and output that works with data spread over several nodes. To do all of the above, we created the `grid` class which forms the backbone of `grim`.

5.3.1. Parallelization

An instance of the `grid` class is created using `grid prim(N1, N2, N3, Ng, dim, Nvar)`⁶, where `N1`, `N2`, and `N3` are the number of grid zones along X^1 , X^2 and X^3 directions respectively, `Ng` is the number of ghost zones required, `dim` is the dimension, and `Nvar` is the number of variables at each zone. This builds a structured grid, performs domain decomposition using PETSc over a chosen number of distributed nodes, and creates `prim.vars[0]`, `prim.vars[1]`, ..., `prim.vars[Nvar-1]`, each of which is an array from the ArrayFire library which lives on either CPUs, or GPUs, depending on the node architecture.

Each array is a contiguous block of memory of size $(N1Local + Ng) \times (N2Local + Ng) \times (N3Local + Ng)$, where `N1Local`, `N2Local` and `N3Local` are the local sizes of the domain on each node. This arrangement of variables in memory is known as Struct of Arrays (SoA), leading to vectorized pointwise operations, and contiguous memory accesses. This results in optimal memory bandwidth usage, which as we discuss in §7 determines `grim`'s performance.

Communication of ghost zones is performed by simply calling `prim.communicate()`, which will exchange ghost zone data of all `Nvar` variables in `prim` using MPI. The `communicate` function works independent of where the data lies, whether on the host CPU or attached GPU(s). If the data is on GPUs, it is transferred to the host, the ghost zone data is exchanged, and transferred back to the GPUs.

6. Performance and Scaling

We have benchmarked `grim` on clusters with varied architectures. On the Stampede supercomputer, using NVIDIA K20 GPUs, `grim` evolves 138,000 grid zones/sec/GPU, with $64 \times 64 \times 64$ zones per GPU. On the CPU nodes which have a 16 core (2 sockets x 8 cores each) Intel Xeon E5-2680 CPU, and the same resolution per node, the performance is 48,000 zones/sec/node. `grim` scales well on both CPU and GPU machines. Fig. 3 shows $\sim 93\%$ weak scaling up to 4096 CPU cores on Stampede, and 256 GPUs on Bluewaters.

The primary difference in speed when using `grim` on GPUs, as compared to CPUs is due to the higher memory bandwidth available on GPUs. The typical accessible bandwidths on GPUs are ~ 140 GB/s, while on CPUs it is ~ 50 GB/s (using all cores on all sockets). Based on this, we expect a single GPU to be $\sim 2 - 3$ times faster than a multicore CPU for

⁶For the exact form of the definitions, please refer to the source code

our implementation.

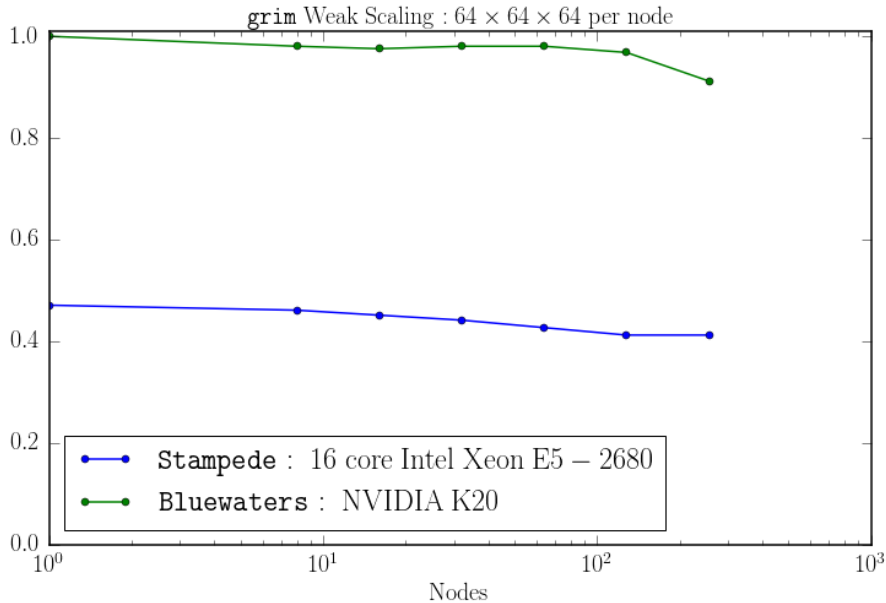


Fig. 3.— Weak scaling on 256 CPU nodes (4096 cores) of Stampede, compared to 256 GPU nodes of Bluewaters. The performance has been normalized to the value of that on a single Bluewaters node. The scaling on both machines is $\sim 93\%$.

7. Performance model

The performance numbers quoted in §6 are *experimental* results. They do not give information regarding the efficiency of our implementation of the algorithms described in (§2 and §3). In order to do so, we require a performance model to benchmark against.

Performance of a code on a given machine is broadly set by two factors, the algorithm, and the implementation. Our root finder (§3) while allowing for the exploration of a broad range of fluid-like theories is much slower (factor of ~ 50 slower per CPU core) than the schemes (Noble et al. 2006) used for primitive variable inversion in ideal relativistic fluids. As a result, the dominant cost in `grim` ($\sim 90\%$) is the nonlinear solver, with the sum of the reconstruction procedure, and the Riemann solver taking only $\sim 5\%$ of the time. Therefore, we focus our efforts on understanding the costs involved in the nonlinear solver.

The nonlinear solver involves the following three steps (1) Jacobian assembly, (2) solu-

tion of a block diagonal linear system, and (3) linesearch. For the linear solver, we use vendor provided LAPACK routines, which we assume are already optimized. Therefore, we only consider the Jacobian assembly and the linesearch, both of which are performed by repeated calls to the residual function $R(P)$. Given a guess for the N_{var} primitive variables P , the $N_{\text{var}} \times N_{\text{var}}$ Jacobian $J(P)$ (eq. 21) is assembled using N_{var} calls to the residual function $R(P)$ (eq. 19) that returns a vector of size N_{var} . Similarly, the linesearch algorithm only depends on the residual function, through its norm $f(\lambda) = \|R(P + \lambda\delta P)\|^2$ (eq. 24). Thus, it is sufficient to analyze the operations involved in the residual function.

7.1. Residual assembly

Consider assembly of the residual $R(P_{n+1/2})$. It is assembled with calls to functions that compute the conserved variables $U(P)$ and the source terms $S^I(P)$, $S(\partial_t P) \equiv A^t(P_n)(P_{n+1/2} - P_n)/(0.5\Delta t)$, each of which return a vector of size N_{var} . The other terms in the residual, $U(P_n)$, $F^{1,2,3}(P_n)$, $S^I(P_n)$, and $A^i(P_n)\partial_i P_n$, only involve P_n , the primitive variables at the previous time step, and are precomputed outside the residual assembly. Therefore, the performance of the residual computation, and hence the Jacobian assembly, and the linesearch are set by the performance of the functions to compute $U(P)$, $S^I(P)$, and $S(\partial_t P)$. We now discuss the main factor that determines the runtime of these functions, the memory bandwidth of the system.

7.1.1. Primary Architectural Bottleneck

Consider the computation of the fluid conserved variables $U(P) \equiv T_\nu^0$, with an ideal MHD stress tensor, for brevity. The computation requires the density $\rho \equiv \text{rho}$, internal energy $u \equiv \text{u}$, pressure $P \equiv \text{P}$, the four-velocities $u^\mu \equiv \text{uCon}$, $u_\mu \equiv \text{uCov}$, the magnetic field four-vectors $b^\mu \equiv \text{bCon}$, $b_\mu \equiv \text{bCov}$, and the magnetic pressure $b^2 \equiv \text{bSqr}$,

```
for (int nu=0; nu < 4; nu++)
{
    T[0][nu] = (rho + u + P + bSqr)*uCon[0]*uCov[nu]
              + (P + bSqr/2)*delta(0, nu)
              - bCon[0]*bCov[nu];
}
```

where $\text{delta}(0, \text{nu}) \equiv \delta_\nu^0$ is the Kronecker delta.

The above code has a total of 11 floating point operations, 14 reads `rho`, `u`, `P`, `bSqr`, `uCon[0]`, `uCov[nu]`, `bCon[0]`, `bCov[nu]`, and four writes `T[0][nu]`. The total time taken to execute the above code is the time taken to load the data, perform the floating point operations, and finally write the data. Therefore, the total time taken is

$$t_{total} = (N_{reads}t_{read} + N_{flops}t_{flops} + N_{writes}t_{write})N \quad (51)$$

where N_{reads} , N_{writes} , and N_{flops} are the total number of reads, writes, and flops performed per grid zone, N is the total number of grid zones, and t_{read} , t_{write} , and t_{flops} is the time taken by the machine to perform a single read, write, and a floating point operation respectively. The parameters t_{read} , t_{write} , and t_{flops} are architecture and machine specific. The specifications are usually given in terms of floating point operations per second *flops*, and memory bandwidth *Bytes/sec*. Typical peak numbers for a current CPU are 500 *Gflops*, and 100 *GB/sec*. For $N \sim 10^9$ (and hence ignoring latency effects), these correspond to $Nt_{flops} \sim 0.02$ seconds, $Nt_{read} \sim 1.12$ seconds, and $Nt_{write} \sim .32$ seconds. Evidently, the ratio $(t_{reads} + t_{writes})/t_{flops} \gg 1$. Therefore, the runtime of the above code is almost completely set by how fast the data can be transferred between the memory system and the compute units. The actual computation time is negligible, as long as $N_{flops}/(N_{reads} + N_{writes}) \sim 1$, which is indeed the case for all functions involved in the Jacobian assembly and the linesearch.

7.1.2. Effective Bandwidth Usage

Since the performance is set by the speed of memory access, we can calculate the time it should take to compute the functions $U(P)$, $S^I(P)$, and $S(\partial_t P)$ by simply examining the inputs N_{reads} , and the outputs N_{writes} to each function. The calculation is independent of the exact operations $P \rightarrow \{U(P), S^I(P), S(\partial_t P)\}$, and is given by

$$t \text{ (secs)} = \frac{(N_{reads} + N_{writes}) \times 8}{10^9} \times \frac{1}{\text{Bandwidth (GB/sec)}} \quad (52)$$

where N_{reads} , and N_{writes} are the number of reads, and writes of double precision variables, each of which are 8 bytes. By measuring the runtime t of each function, the *effective* bandwidth being used is calculated using (52).

The measured bandwidth used in each function is now normalized with that obtained from the **STREAM** benchmark, given by the operation $\mathbf{c} = \mathbf{a} + \mathbf{b}$, where \mathbf{a} , \mathbf{b} , and \mathbf{c} are arrays of sizes equal to the local grid sizes after domain decomposition. The **STREAM** benchmark has $N_{reads} = 2$ (\mathbf{a} , \mathbf{b}), $N_{writes} = 1$ (\mathbf{c}), and is a metric of the sustained bandwidth that can be obtained on a given machine. The typical value of this benchmark on GPUs is ~ 140

GB/sec, whereas on CPUs it is ~ 50 GB/sec for array sizes that exceed the cache, and when using all cores on all sockets ⁷. These numbers inform us about the potential speedup of bandwidth limited operations on GPUs, compared to CPUs.

By comparing the measured bandwidth of each function to the bandwidth obtained from the **STREAM** benchmark, we get the efficiency of our implementation, which we find is $\sim 70 - 80\%$ on both GPUs and CPUs. A significantly lower ($\lesssim 20\%$) value indicates that there are either superfluous memory accesses that are not accounted for, or non-contiguous memory accesses that are not vectorized. Both of these reduce the effective memory bandwidth. The high bandwidth obtained by our implementation indicates that we have accounted for leading order performance bottlenecks in the residual evaluation, leading to a near-optimal Jacobian assembly and linesearch.

8. Test Suite

grim has been tested extensively in the linear, nonlinear, special and general relativistic regimes. The tests below are grouped according to the physical model being solved, with subsections describing individual tests.

8.1. Extended MHD

8.1.1. Linear modes

An important check of any numerical implementation of the EMHD model is whether it can reproduce the corresponding linear theory with an error that falls off at the expected order of spatio-temporal discretization. In order to perform this test, one needs the linear theory of the EMHD model.

The governing equations of EMHD are considerably more complicated than the governing equations of ideal MHD. In particular the inclusion of both anisotropic pressure and conduction, which are sourced by spatio-temporal derivatives projected along the magnetic field lines, make it challenging to derive the linear theory; the derivation is prone to errors

⁷Comparing a single CPU core to an entire GPU is not representative of how CPUs are used in production runs. Using a single core of a CPU leads to bandwidths that are much lower than the peak. In order to saturate the bandwidth, it is *necessary* to use $\gtrsim 50\%$ of all available cores.

if done manually. To address this issue, we have written a general linear analysis package ⁸ built on top of the SageMath (2016) computer algebra system, which takes as input the governing equations of any model, and generates the characteristic matrix of the corresponding linear theory. The eigenvectors of this matrix are then used as initial conditions in `grim`, and their numerical evolutions checked against the corresponding analytic solutions.

Variable (P)	Background State (P_0)	Perturbed Value (δ_P)
ρ	1.	$-0.518522524082246 - 0.1792647678001878i$
u	2.	0.5516170736393813
u^1	0.	$0.008463122479547856 + 0.011862022608466367i$
u^2	0.	$-0.16175466371870734 - 0.034828080823603294i$
u^3	0.	$0.$
B^1	0.1	$-0.05973794979640743 - 0.03351707506150924i$
B^2	0.3	$0.02986897489820372 + 0.016758537530754618i$
B^3	0.	$0.$
q	0.	$0.5233486841539436 + 0.04767672501939603i$
ΔP	0.	$0.2909106062057657 + 0.02159452055336572i$

Table 1: Eigenvector with eigenvalue for EMHD linear modes test.

Our linear test uses a propagating mode with wave vector $k_1 = 2\pi, k_2 = 4\pi$ misaligned with the background magnetic field $\mathbf{B}_0 = (0.1, 0.3, 0)$. Both \mathbf{k} and \mathbf{B} are misaligned with the numerical grid. We use the eigenvector tabulated in table (8.1.1). Each of the variables are initialized as $P = P_0 + A\delta_P \exp(i(k_1x^1 + k_2x^2))$, where P is the variable, P_0 is the background state, δ_P is the perturbed values, and A is the amplitude of the perturbation, which we set to 10^{-8} . The exact solution is given by $P = P_0 + A\delta_P \exp(i(k_1x^1 + k_2x^2) + \omega t)$, where $\omega = -0.5533585207638141 - 3.6262571286888425i$. The mode is both propagating and decaying, indicating the presence of dissipation.

The mode is evolved in a box with dimensions $[0, 1] \times [0, 1]$, periodic boundary conditions, and resolutions $(N_1, N_2) = (32, 32), (64, 64), \dots, (512, 512)$. The diffusion coefficients are $\chi = c_s^2\tau_R$, and $\nu = c_s^2\tau_R$, with $\tau_R = 1, c_s^2 = \gamma P / (\rho + \gamma u), P_g = (\gamma - 1)u$, and $\gamma = 4/3$. We compare the numerical and analytic solutions at $t = 0.5$. Fig. 4 shows that the L_1 norm of the error falls off at the expected order.

⁸balbusaur: <http://bit.ly/2bEGW41>

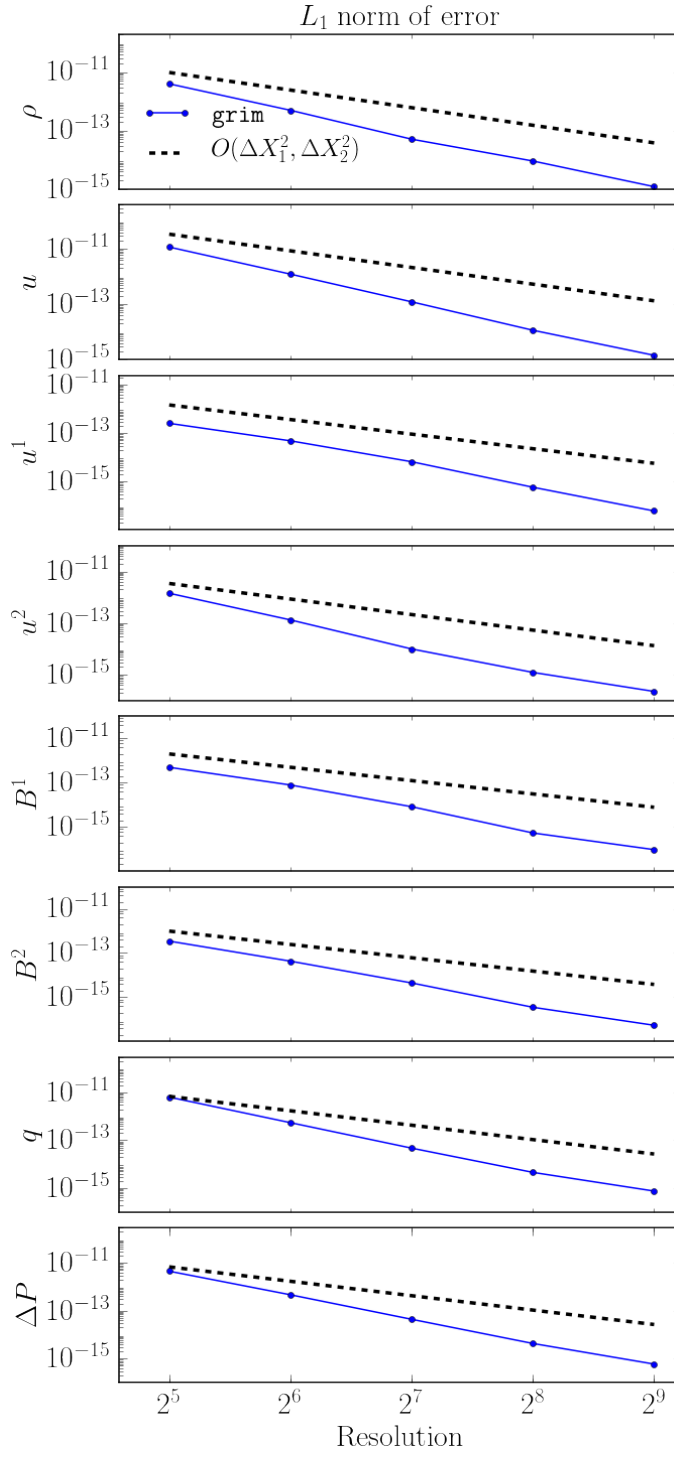


Fig. 4.— Convergence in the linear modes test.

8.1.2. EMHD Shock Solutions

In EMHD, viscosity can smooth a shock and connect the left and right states with a well-defined solution. The hyperbolic nature of the dissipation leads to new features in the shock structure which have been qualitatively described in Chandra et al. (2015). Here, we solve the magnetic field aligned shock structure in the EMHD model as a boundary value problem (BVP) with the left and right states fixed to the values given by the Rankine-Hugoniot jump conditions. We then use this as a reference solution to check the EMHD shock solutions obtained from `grim`, which solves the EMHD equations as an initial value problem (IVP) (fig. 5).

The boundary value solutions are obtained using a global Newton root finder. We are looking for a steady state time independent nonlinear solution of the EMHD equations, and hence set the time derivatives $\partial_t \rightarrow 0$. Since we are interested in the *continuous* shock sub-structure, we approximate all spatial derivatives ∂_x by central differences with a truncation error $O(\Delta x^8)$. Thus we have a set of coupled discrete nonlinear equations $R(P_i) = 0$, where P_i are the primitive variables at $i = 0, 1, \dots, N_x$, and N_x is the chosen spatial resolution of the numerical grid. The system is iterated upon starting from a smooth initial guess using the Newton’s method combined with a numerical Jacobian assembled to machine precision. The iterations are continued until we achieve machine precision error $O(10^{-14})$.

The solution obtained from the initial value problem starting from a discontinuous initial condition (shown in table (8.1.2)), and the solution obtained from the boundary value problem are connected by a translation. For a quantitative check of the error, we use the BVP solution as an initial condition into `grim`, and check for convergence after a fixed time. Fig. 6 shows convergence between the two solutions as a function of resolution.

Variable	Left State	Right State
ρ	1.	3.08312999
u	1.	4.94577705
u^1	1.	0.32434571
u^2	0.	0.
u^3	0.	0.
B^1	10^{-5}	10^{-5}
B^2	0.	0.
B^3	0.	0.

Table 1: Steady state shock solution in Ideal MHD

The EMHD theory has three free parameters which we set to the following values:

the relaxation time scale $\tau_R = 0.1$, the kinematic viscosity $\nu = \psi c_s^2 \tau_R$, and the thermal diffusivity $\chi = \phi c_s^2 \tau_R$, with the non-dimensional parameters $\psi = 3$ and $\phi = 5$. To get a continuous shock solution we require that the characteristic speed of viscosity in the EMHD theory $v_{\text{char}} \sim (\nu/\tau_R)^{1/2} = \psi^{1/2} c_s$ be greater than the upstream velocity, here $v^1 = u^1/u^0$ in the left state. Thus, we require $v_{\text{char}} > v^1 \implies \psi > (v^1/c_s)^2$. For our chosen set of parameters we have $v_{\text{char}} \approx 0.756 > v^1 \approx 0.707$, and hence we are able to resolve the shock structure. We find that the major contribution to the shock structure comes from the pressure anisotropy; the role of the heat conduction inside the shock is marginal. The EMHD theory has hyperbolic dissipation, where q and ΔP relax to values $q_0 \propto \nabla_\mu T$, $\Delta P_0 \propto \nabla_\mu u_\nu$ over a time scale τ_R . This leads to structure of length $\sim v^1 \tau_R$ over which the dissipation builds up (figure 5), and then reaches the relaxed values $q_0, \Delta P_0$. The theory has higher order corrections $\sim q u^\mu \nabla_\mu (\tau_R/(\chi P^2)), \Delta P u^\mu \nabla_\mu (\tau_R/(\rho \nu P))$ that we expect to contribute in strong nonlinear regimes, and indeed we see that the shock structure differs as we turn on, and turn off, these terms (fig. 7). However, from fig. 7, we see that the differences are small. Still, their presence is required to enforce the second law of thermodynamics.

There is an upper limit to the strength of the shock that can be solved for using the EMHD model. Higher mach number shocks require a larger viscosity (or ΔP) to smoothly connect the left and right states. However, the non-dimensional parameter ψ cannot be arbitrarily large because of an upper bound on the associated characteristic speed $v_{\text{char}} \sim \psi^{1/2} c_s < c \implies \psi < (c/c_s)^2$. Beyond this critical value, the theory loses hyperbolicity, and eventually causality and stability. The root of this problem lies in the fact that ultimately, the theory is a second order perturbation $\sim q^2, \Delta P^2$, about an equilibrium and, as the dissipative effects become stronger, the validity of the expansion breaks down.

What happens if we do not resolve the shock? In astrophysical applications, this is almost always the case since there is a large separation between the MHD, and the kinetic spatio-temporal scales. The pressure anisotropy ΔP is limited to the values allowed by the saturation of kinetic instabilities such as mirror and firehose. For example $\Delta P \sim b^2$, where b^2 is the magnetic pressure. This viscosity may not be sufficient to resolve a shock. However, since **grim** is a conservative code, even when shocks are not resolved, the obtained solution asymptotes to the value given by the ideal fluid Rankine-Hugoniot jump conditions a few mean free paths away from the shock.

8.1.3. Anisotropic Conduction Test

The EMHD model constrains heat to flow only along the magnetic field lines $q_0 \propto \hat{b}^\mu (\nabla_\mu T + T a_\mu)$. To test this, we set up a temperature perturbation in pressure equilibrium,

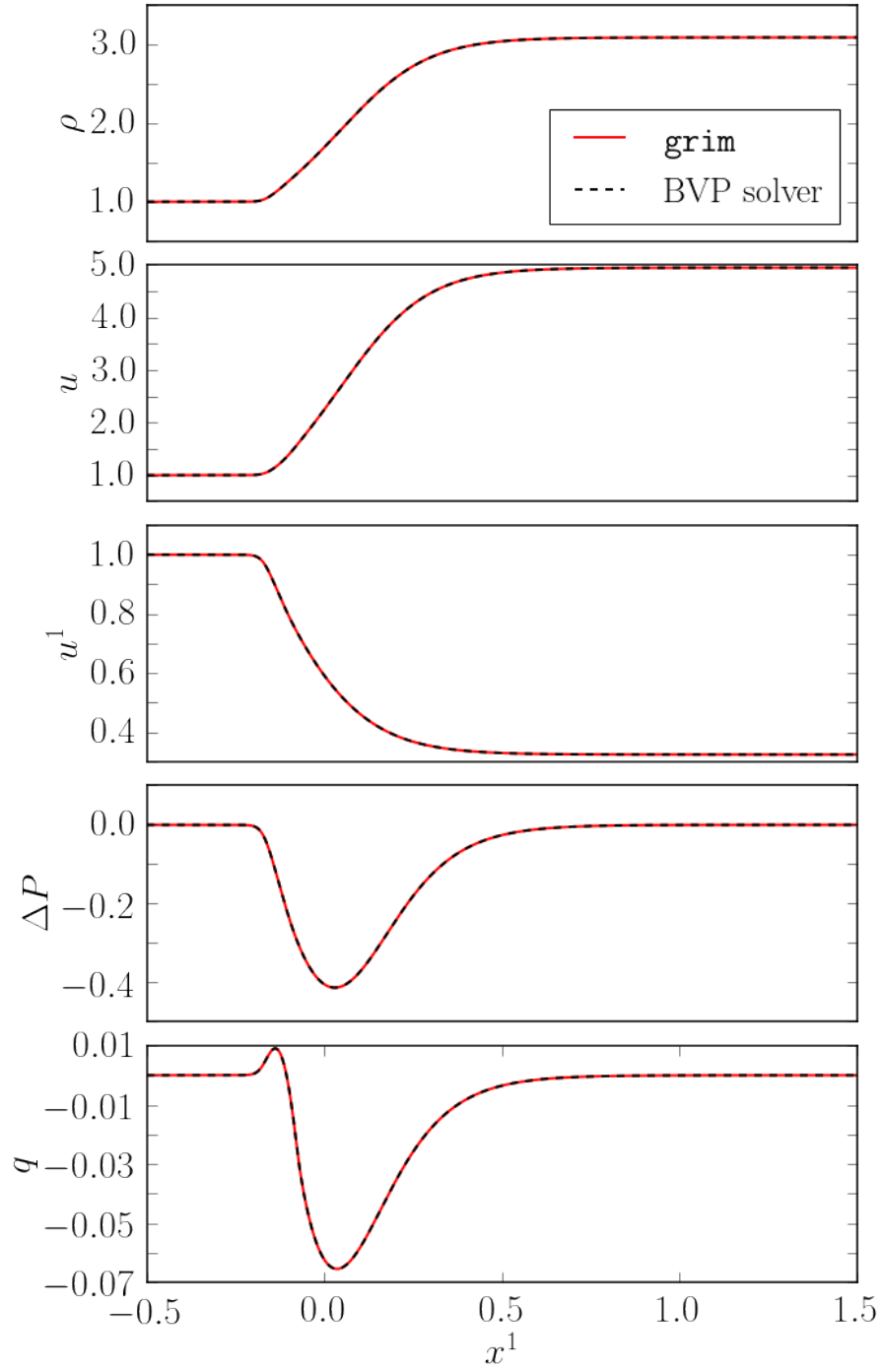


Fig. 5.— Shock solution obtained by `grim`, which solves the EMHD theory as an initial value problem (IVP), plotted on top of the shock solution of the EMHD theory, solved as a boundary value problem (BVP).

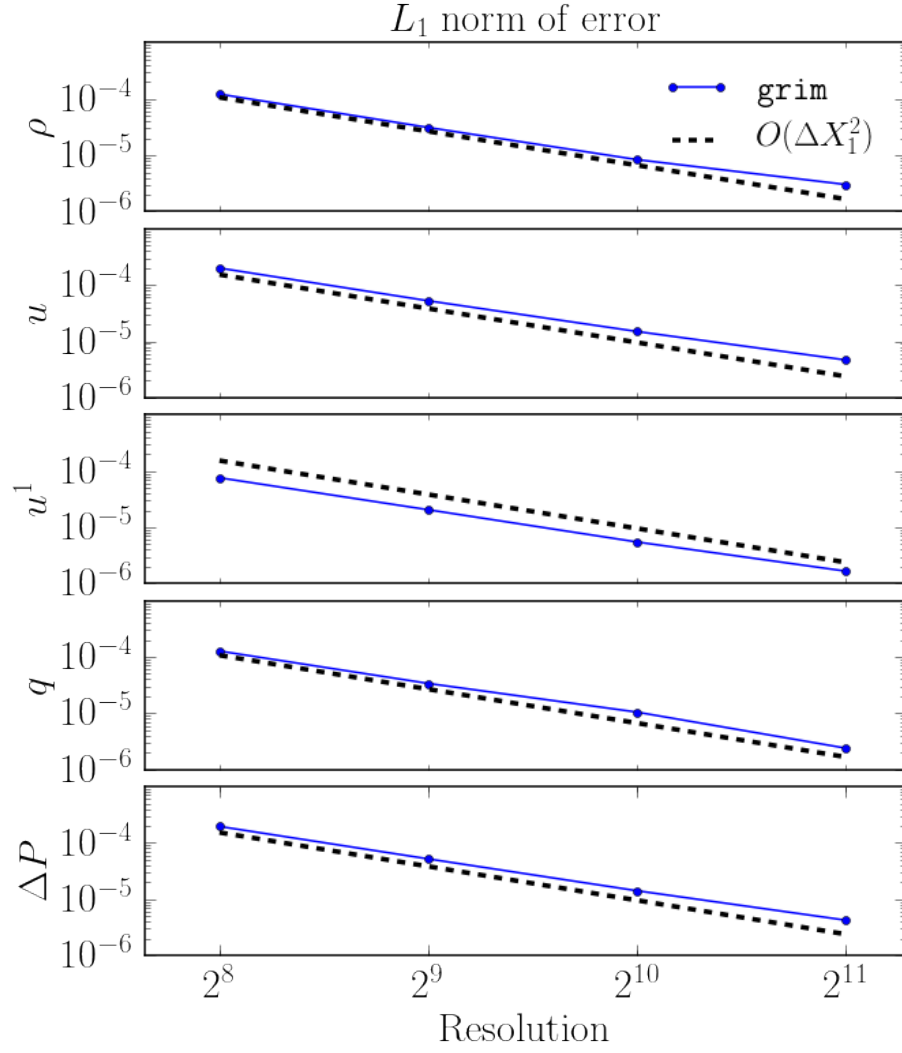


Fig. 6.— Convergence of a resolved EMHD shock, between an initial value problem solved with `grim`, and a boundary value problem solved by setting $\partial_t \rightarrow 0$ in the EMHD theory.

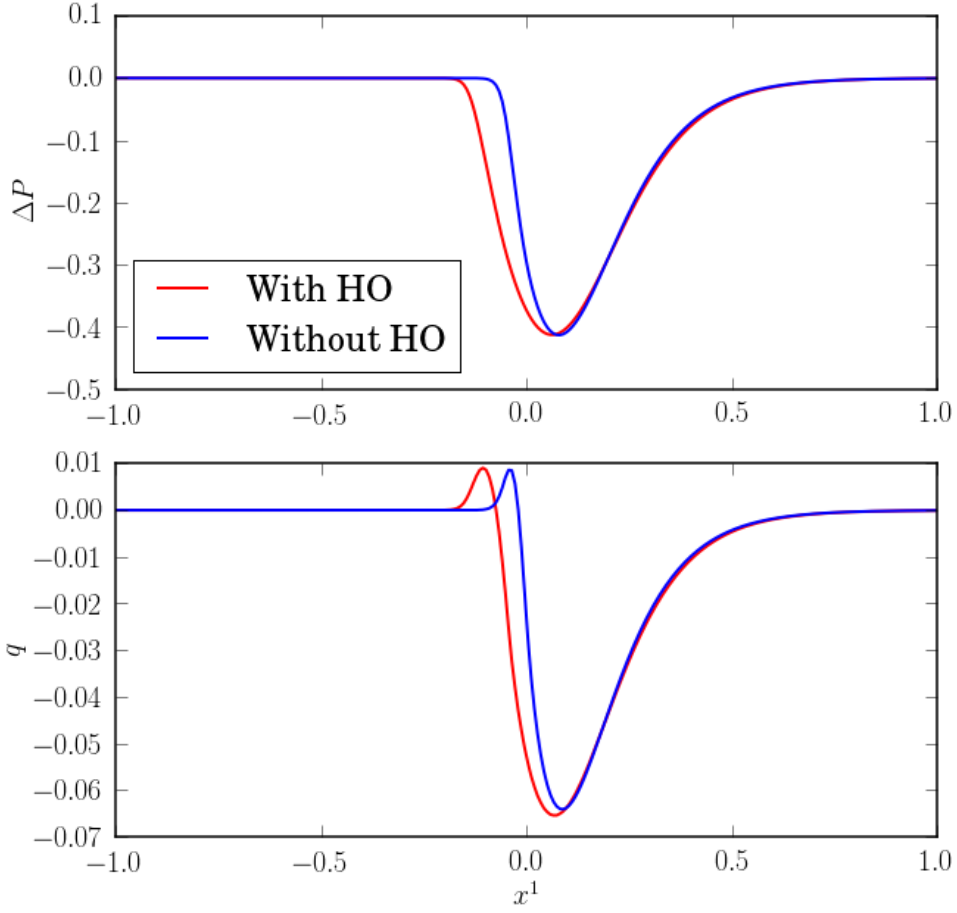


Fig. 7.— Dependence of the shock substructure on the presence of higher order (HO) terms $\sim qu^\mu \nabla_\mu(\tau_R/(\chi P^2)), \Delta P u^\mu \nabla_\mu(\tau_R/(\rho \nu P))$ in the EMHD theory.

in Minkowski space-time with sinusoidal background magnetic field lines. The domain is a square box of size $[0, 1] \times [0, 1]$ with periodic boundary conditions. The initial conditions are

$$\rho = 1 - Ae^{-r^2/R^2} \quad (53)$$

$$u = 1 \quad (54)$$

$$u^1 = u^2 = u^3 = 0 \quad (55)$$

$$B^1 = B_0 \quad (56)$$

$$B^2 = B_0 \sin(2\pi kx^1) \quad (57)$$

where the amplitude of the perturbation $A = 0.2$, the radius $R = \sqrt{.005}$, the mean magnetic field $B_0 = 10^{-4}$, and the wavenumber of the magnetic field $k = 4$. The adiabatic index is set to $\gamma = 4/3$, the relaxation time scale in the EMHD model $\tau_R = 0.1$, and the thermal diffusivity $\chi = 0.01$.

Since the initial conditions are in pressure equilibrium, they are an exact time independent solution of the ideal MHD equations. However, the EMHD model is sensitive to temperature gradients along field lines, and hence the system should evolve to a state where the plasma becomes isothermal along field lines. This outcome is shown in fig. 8, along with the transient state. As the heat flows, it excites sound waves that traverse the domain, eventually reaching the steady solution shown in the last panel in fig. 8.

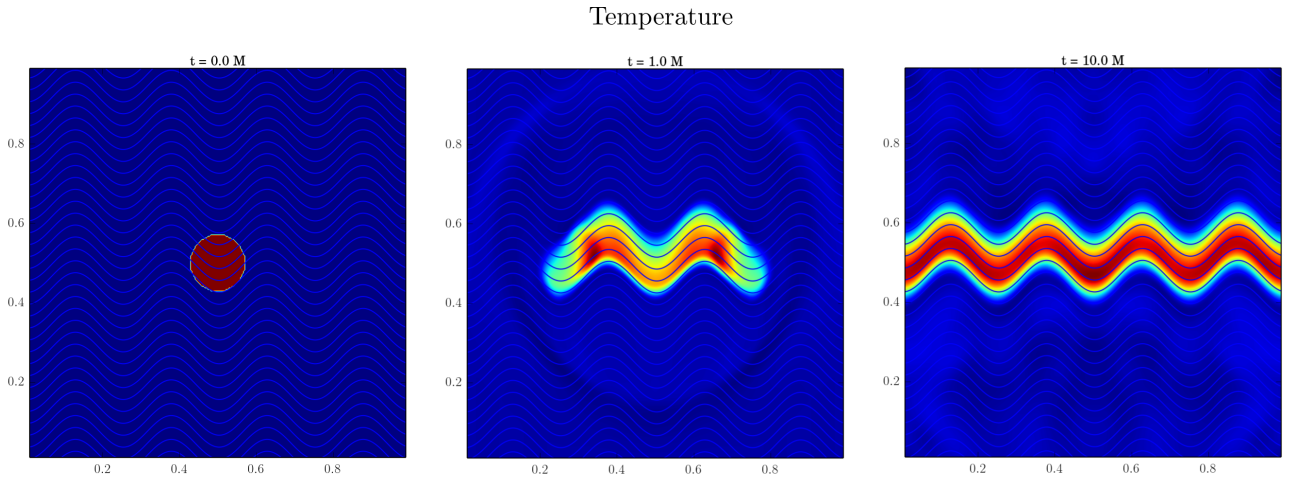


Fig. 8.— Evolution of a temperature perturbation, initially in pressure equilibrium, over sinusoidal magnetic field lines. This test provides a nice visualization of the anisotropic transport of the EMHD theory.

8.1.4. Firehose Instability

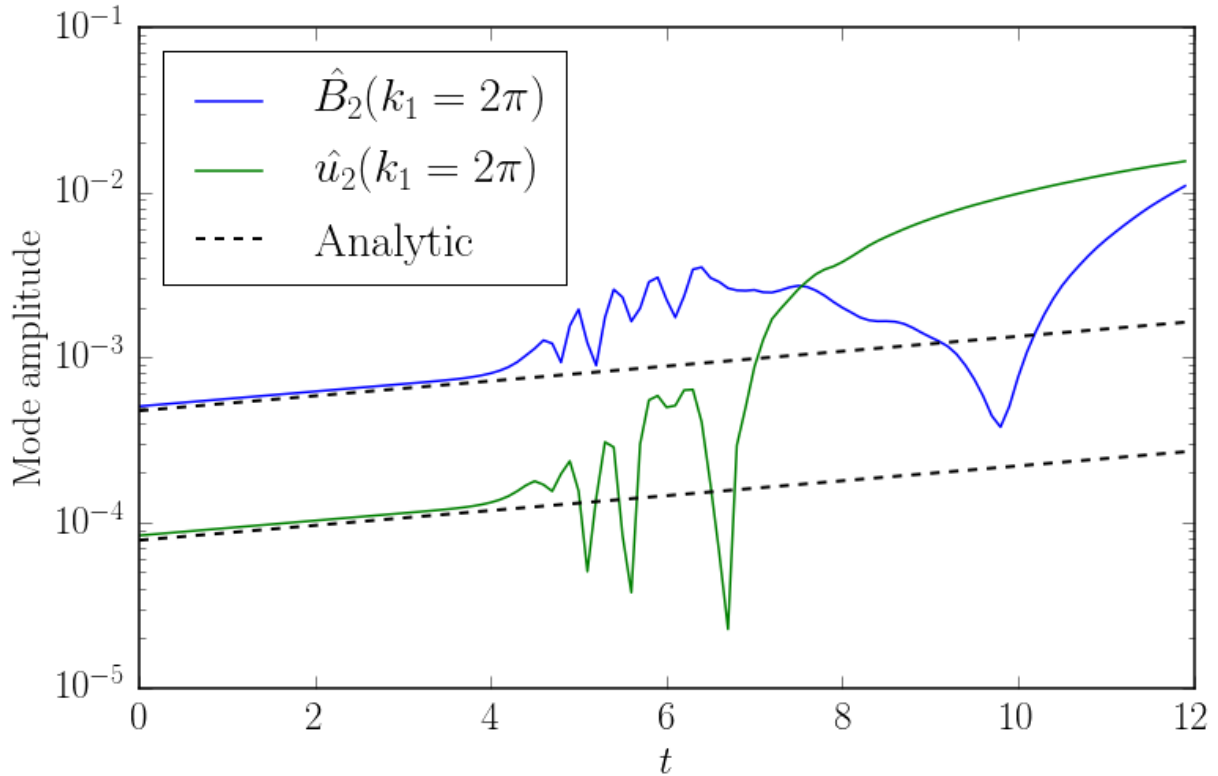


Fig. 9.— Mode growth in the firehose instability test.

The EMHD model, like Braginskii’s theory of weakly collisional anisotropic plasmas, is susceptible to the firehose instability. If $\Delta P < -b^2$ Alfvén waves become unstable and grow at a rate proportional to their wavenumber (see Chandra et al. (2015) for the EMHD result). To test the linear growth of a firehose-unstable mode, we consider the following

initial conditions on a Minkowski background:

$$\rho = 1 \tag{58}$$

$$u = 2 \tag{59}$$

$$u^1 = u^3 = 0 \tag{60}$$

$$u^2 = A \sin(2\pi x^1) \tag{61}$$

$$B^1 = 0.1 \tag{62}$$

$$B^2 = B \cos(2\pi x^2) \tag{63}$$

$$B^3 = 0 \tag{64}$$

$$\Delta P = -0.011 \tag{65}$$

with $A = 0.1628\alpha$ and $B = 0.9867\alpha$ chosen so that the perturbation of amplitude α is one of the linearly unstable Alfvén modes, with exponential growth rate $\Gamma = 0.1036$. We artificially impose a very slow damping rate $\tau_R = 10^6$ to the pressure anisotropy, to avoid rapid damping of the imposed pressure anisotropy ΔP towards its equilibrium value $\Delta P \approx 0$ (as the background flow has no shear).

In Fig. 9 we show the evolution of the unstable mode amplitude. We observe two separate regimes of evolution. First, the unstable mode grows exponentially at the predicted rate Γ , in agreement with the linear theory. At later times truncation error seeds perturbations on smaller length scale, which have a much faster growth rate. Around $t = 4$ the growth of the perturbation is dominated by grid-scale modes, which grow much faster than the mode we inserted in the initial conditions, and quickly become nonlinear.

In kinetic theory, the pressure anisotropy saturates at $\Delta P \approx -b^2$. In astrophysical simulations, we similarly impose a saturation of ΔP by smoothly reducing τ_R if $\Delta P < -b^2$.

8.1.5. Hydrostatic Conducting Atmosphere

Heat conduction in curved space-times contains qualitatively new features when compared to Minkowski space-time because the heat flux is driven by *red-shifted* temperature gradients $q_0 \propto \hat{b}^\mu (\nabla_\mu \Theta + \Theta a_\mu)$ where $a^\lambda = u^\nu \nabla_\nu u^\lambda \equiv u^\nu \partial_\nu u^\lambda + \Gamma_{\mu\nu}^\lambda u^\mu u^\nu$ is the four-acceleration. For a fluid at rest in a stationary spacetime this simplifies to $q_0 \propto \partial_i(\Theta \sqrt{-g_{00}})/\sqrt{-g_{00}}$. Thus, a zero heat flux configuration corresponds to $\partial_i(\Theta \sqrt{-g_{00}}) = 0$, and not $\partial_i \Theta = 0$. A fluid element deep in a gravitational potential well requires greater internal energy in order to stay in thermal equilibrium with a fluid element outside the potential well. We test this effect with a hydrostatic fluid configuration in a Schwarzschild metric in the domain

$(R, \theta) = [200 M, 300 M] \times (0, \pi/2)$. The equations of hydrostatic equilibrium are

$$\frac{\partial P}{\partial x^1} = -(\rho + u + P) \frac{\partial \ln \sqrt{-g_{00}}}{\partial x^1} \quad (66)$$

$$\frac{\partial(q\sqrt{g^* g_{00}})}{\partial x^1} = \sqrt{-g} T_{\lambda}^{\kappa} \Gamma_{\nu\kappa}^{\lambda} \quad (67)$$

$$\frac{\partial(\Theta\sqrt{-g_{00}})}{\partial x^1} = q \quad (68)$$

where (66) is the momentum conservation equation in the radial direction, (68) is the energy equation, and (67) is the evolution equation for the heat flux (35), simplified in the presence of a radial magnetic field, and the absence of a radial velocity ($u^r = 0$). The above equations are one-dimensional ODEs in the radial direction which we integrate outwards between two concentric spheres, starting with (P_0, Θ_0, q_0) at the inner boundary. The above equations are augmented by the ideal gas equation of state $u = P_g/(\gamma - 1)$, with $\gamma = 4/3$, and $\rho = P/\Theta$ to determine u and ρ respectively. The resulting (semi-)analytic solutions are then used as initial conditions in **grim**. If the numerical implementation is correct, **grim** should maintain the equilibrium. We consider two cases, (1) $q_0 = 0 \implies q = 0$, which is a system in thermal equilibrium, and (2) $q_0 \neq 0 \implies q \neq 0$, corresponding to a system that is conducting heat radially outwards. Fig. 10 shows the errors at the final time of the evolution falling off at the expected order for both cases.

8.1.6. Bondi Inflow

Spherical accretion onto a non-spinning black hole is a common test of general relativistic hydrodynamics code. It is a rare case of a non-trivial configuration for which a steady-state solution can be obtained analytically. For this test, we use as background flow the well-known solution for a spherical accretion flow around a non-spinning black hole of mass $M = 1$ due to Michel 1972. This solution has a sonic point which we place at $r_s = 8GM/c^2$. We also add a radial magnetic field $B^r = 1/\sqrt{-g}$, which does not modify the hydrodynamics equilibrium.

The Bondi inflow solution has a non-trivial u^r . The presence of a finite inflow velocity exercises all the time-independent terms in the EMHD equations for q and ΔP , including higher order terms that are identically zero in a hydrostatic solution. We obtain reference solutions by ignoring backreaction of the dissipation onto the fluid flow and integrate one-dimensional ODEs in the radial direction for q and ΔP . We then use these solutions to check **grim** results obtained with backreaction turned off.

Fig. 11 shows the value of the pressure anisotropy obtained at time $t = 1000GM/c^3$

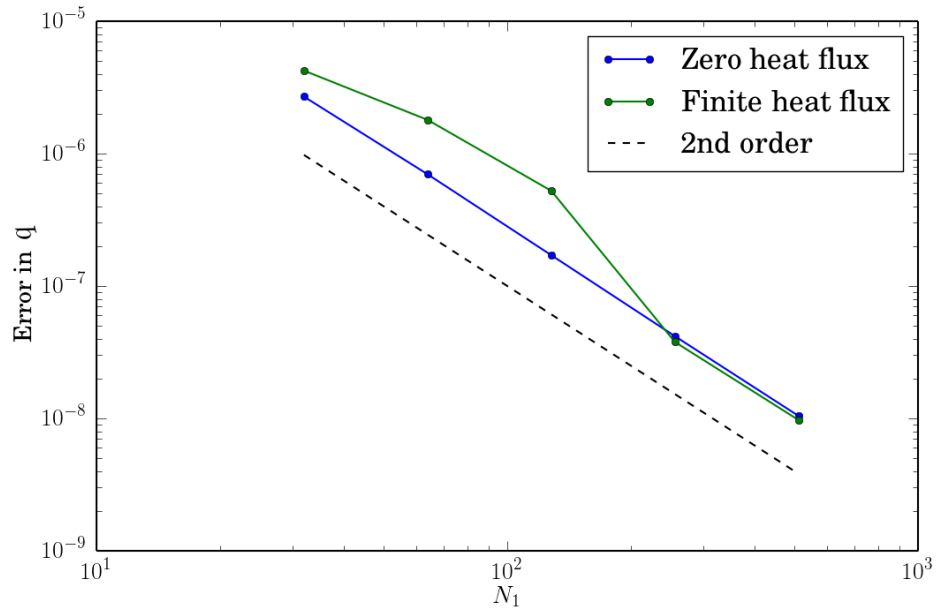


Fig. 10.— Convergence for a hydrostatic atmosphere with zero, and finite heat flux at $t = 10 GM/c^3$.

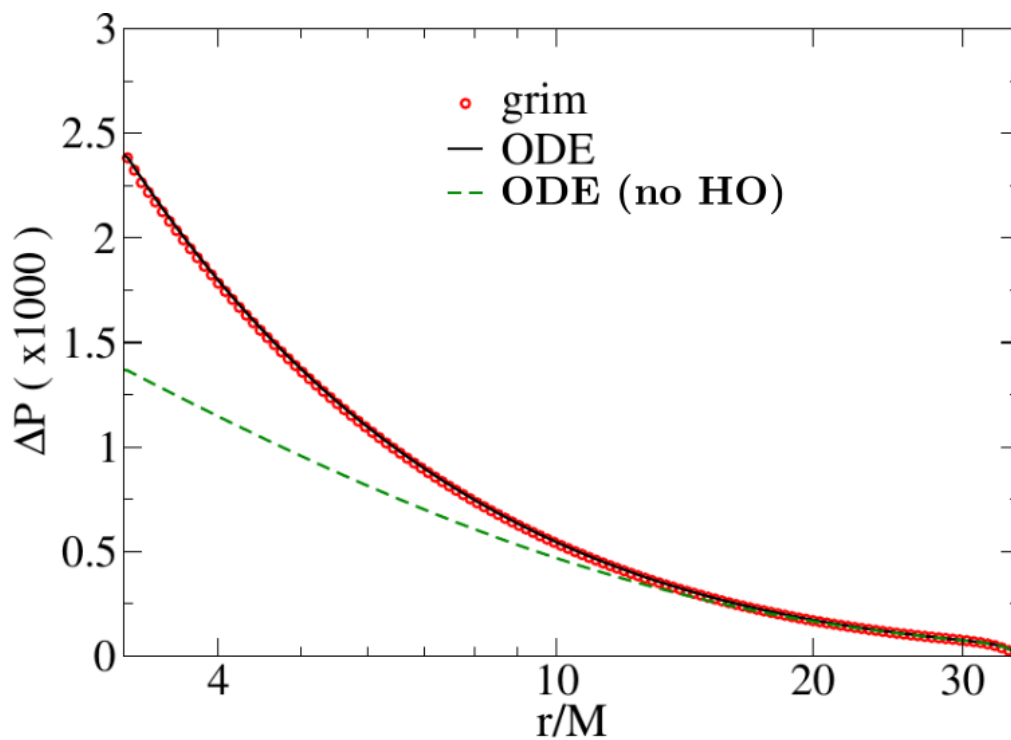


Fig. 11.— Pressure anisotropy at $t = 1000GM/c^3$ for a `grim` evolution of spherical accretion in the EMHD model, without backreaction of the pressure anisotropy onto the flow (red circles). A numerical integration of the analytical solution is shown as a solid black line. The analytical solution without higher order (HO) terms (i.e. simply damping the advected ΔP to ΔP_0 on a timescale τ_R) is shown as a dashed green line.

of a `grim` evolution, and from the simpler ODE integration on top of the steady-state fluid background. The two are in very good agreement. We also note that spherical accretion is an interesting case in which the high-order terms in the evolution of q and ΔP and choice of damping timescale τ_R do change the flow by order unity. Indeed, the rescaled pressure anisotropy $\Delta\tilde{P}$ is damped towards its relaxed value in Braginskii’s theory ($\Delta\tilde{P}_0$), as well being advected with the flow. In this test problem, the pressure anisotropy varies rapidly with radius, but the radial velocity of the flow is also large. For $\tau_R \gtrsim r/u^r$, the pressure anisotropy can thus remain significantly smaller than its Braginskii target. Fig. 11 uses $\tau_R = 30$ everywhere.

8.2. Ideal MHD Tests

EMHD reduces to ideal MHD in the limit of vanishing diffusion coefficients ($\chi, \nu \rightarrow 0$), resulting in zero dissipation ($q, \Delta P \rightarrow 0$)⁹ Therefore, any code that solves the EMHD equations should also be able to handle ideal MHD. To check this, we subject `grim` to ideal MHD shock tests in order to check its shock capturing ability. To solve the ideal MHD equations, we simply ignore the evolution of the heat flux (39), and the pressure anisotropy (40), as well as the relevant terms in the stress-energy tensor (27). This leads to the assembly, and inversion of a 5×5 Jacobian (for the variables $\{\rho, u, u^1, u^2, u^3\}$) in the residual-based root finder, as opposed to a 7×7 Jacobian for EMHD.

We have successfully tested `grim` on the following ideal MHD problems 1) Komissarov (1999) shock tests, 2) relativistic Orzag-Tang (Beckwith & Stone 2011), 3) diagonal transport of an overdensity (Gammie et al. 2003), 4) low, and medium magnetized cylindrical blast wave (Komissarov 1999), 6) steady-state hydrodynamic torus (Fishbone & Moncrief 1976). The Riemann solver in `grim` is identical to that used in `harm`, therefore we are prone to all of the known issues of the `harm` scheme. Specifically, the Local Lax Friedrichs (LLF) flux that we use leads to excess diffusion at contact discontinuities when compared to schemes that explicitly model the discontinuity, like HLLC (Toro et al. 1994).

⁹The limits $\chi, \nu \rightarrow 0$ need to be taken carefully because diffusion coefficients appear in the denominator of the higher order terms ($\sim \tilde{q}\nabla_\mu u^\mu, \Delta\tilde{P}\nabla_\mu u^\mu$) in (39), and (40), where $\tilde{q} \sim q/\sqrt{\chi}, \Delta\tilde{P} \sim \Delta P/\sqrt{\nu}$. To obtain the correct limit, rescale (39) by $\sqrt{\chi}$, and then take $\chi \rightarrow 0$, leading to $q \rightarrow 0$. The limit $\Delta P \rightarrow 0$ follows similarly.

8.2.1. Komissarov shock tests

Komissarov (1999) formulated a series of one-dimensional nonlinear MHD solutions that are designed to check a codes ability to correctly handle shocks and rarefactions. We ran the following cases: (1) fast shock, (2) slow shock, (3) switch-off fast, (4) switch-on slow, (5) shock-tube 1, (6) shock tube 2, and (7) collision. We ran each case with 2048 grid zones in a domain $[-2, 2]$ with a minmod limiter (which in our implementation is the generalized minmod limiter, with slope set to one), and a courant factor of 0.2. As is shown in Fig. 12, we correctly reproduce the expected results.

9. Applications

We describe three example applications that highlight the new physics in the EMHD model: (1) Buoyancy instabilities in weakly collisional plasmas and (2) radiatively inefficient accretion flows around supermassive black holes. We study these in global 3D domains using coordinates by Tchekhovskoy et al. (2011); Tchekhovskoy & Nemmen (2016) that smoothly cylindrify the grid zones near the poles. This mollifies the severe time step constraints in the azimuthal (ϕ) direction.

9.1. Buoyancy Instabilities

Weakly collisional plasmas are subject to instabilities not present in ideal plasmas, due to the presence of anisotropic dissipation. An ideal plasma that satisfies the Schwarzschild criterion $ds/dz > 0$ is convectively stable. However, this is not the case when the heat flux is constrained to be parallel to magnetic field lines.

- When the temperature *decreases* outwards $dT/dz < 0$ against gravity in the presence of magnetic field lines that are *perpendicular* to the temperature gradient¹⁰, the plasma is unstable to the *Magneto-Thermal Instability* (MTI) (Balbus 2000).
- When the temperature *increases* outwards $dT/dz > 0$ against gravity in the presence of magnetic field lines that are *parallel* to the temperature gradient¹¹, the plasma is unstable to the *Heat flux driven Buoyancy Instability* (HBI) (Quataert 2008).

¹⁰When the field lines are aligned along the negative temperature gradient $dT/dz < 0$, the system is MTI stable.

¹¹When the field lines are aligned perpendicular to the positive temperature gradient $dT/dz > 0$, the

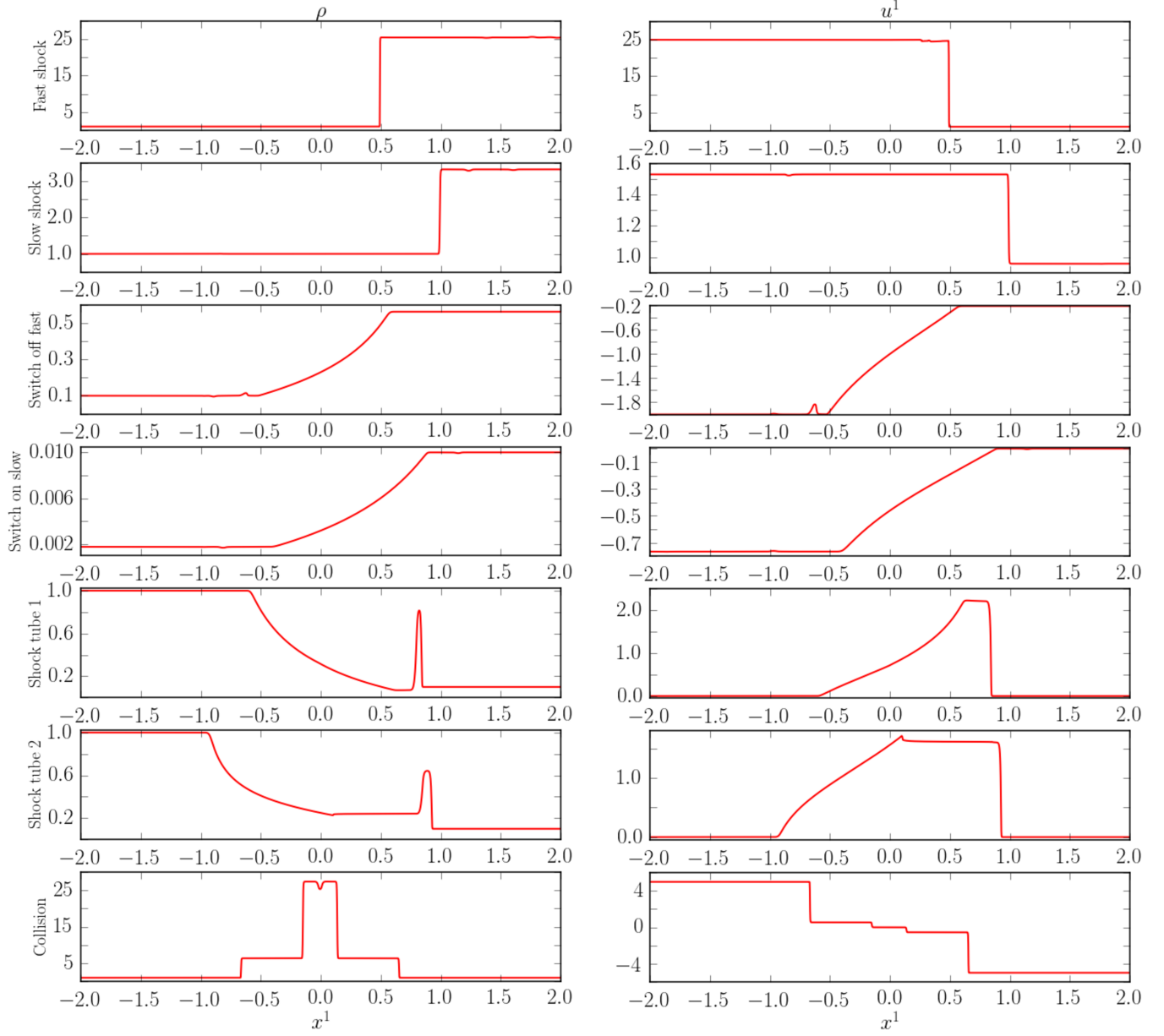


Fig. 12.— Density ρ (left panel), and four-velocity u^1 (right panel) for each of the Komissarov shock tests.

Both instabilities require weak magnetic fields, else they are suppressed by strong magnetic tension. The linear growth and nonlinear saturation of these instabilities have been studied in-depth in the non-relativistic regime using the Braginskii 1965 model for weakly collisional plasmas. The EMHD model reduces to the Braginskii model in the non-relativistic limit when $\tau_R \rightarrow 0$. We expect to see the MTI and the HBI in the EMHD model, and indeed we do. Below we describe the setups and the linear and the nonlinear regimes for both instabilities.

We use hydrostatic Schwarzschild-stable initial conditions in a Schwarzschild metric. We want to be able to control the sign of the temperature gradient, so that the system is either MTI or HBI unstable. To do so, we set the initial $P_g = K\rho^\Gamma$, where K is a constant, and Γ is the polytropic index. P is solved for using hydrostatic equilibrium (66), which then yields $\rho = (P_g/K)^{1/\Gamma}$ and u , using $u = P_g/(\gamma - 1)$.

A Schwarzschild stable equilibrium requires $ds/dr > 0 \implies \Gamma < \gamma$. Γ can be changed to obtain either a positive temperature gradient $dT/dr > 0$ ($\Gamma < 1$), or a negative temperature gradient $dT/dr < 0$ ($\Gamma > 1$). For MTI, we set $K = 10^{-4}$ and $\Gamma = 4/3$, while for HBI we set $K = 0.05$ and $\Gamma = 1/2$.

We set $\chi = c_s R$, where R is radius and $c_s = \sqrt{\gamma P/\rho}$, as in Sharma et al. 2008. The EMHD model has an additional parameter, the relaxation time scale, set via $\tau_R = R/c_s$.

9.1.1. Magneto-Thermal Instability

The MTI requires magnetic field lines perpendicular to the temperature gradient for maximal growth. Therefore, we perform the simulation in a half sphere $(R, \theta, \phi) \in [200M, 300M] \times (0, \pi) \times [0, \pi]$, and initialize with a weak azimuthal magnetic field $B_\phi = 10^{-3}/\sqrt{-g}$. We use Dirichlet boundary conditions in R , and θ for the density ρ , pressure P , and internal energy u . This results in constant temperature boundaries, which continuously drive the instability. We use insulating boundary conditions for the magnetic fields, i.e. set them to zero in the boundaries. The ϕ boundaries are periodic for all variables.

The initial conditions have zero heat flux $q = 0$, as well as $q_0 \sim \hat{b}^\mu (\nabla_\mu \Theta + \Theta a_\mu) = 0$. We seed the simulation with small amplitude, $\sim 4\%$, fluctuations in u^1 . These lead to small scale corrugations of the field lines whose radial component is exponentially amplified due to the MTI (14a). Eventually, there is vigorous convection (fig. 13a), and a net heat flux between the radial boundaries, leading to a flattened temperature profile in the bulk of the domain

system is HBI stable.

(fig. 15). This is consistent with expectations from nonlinear evolution of the nonrelativistic MTI.

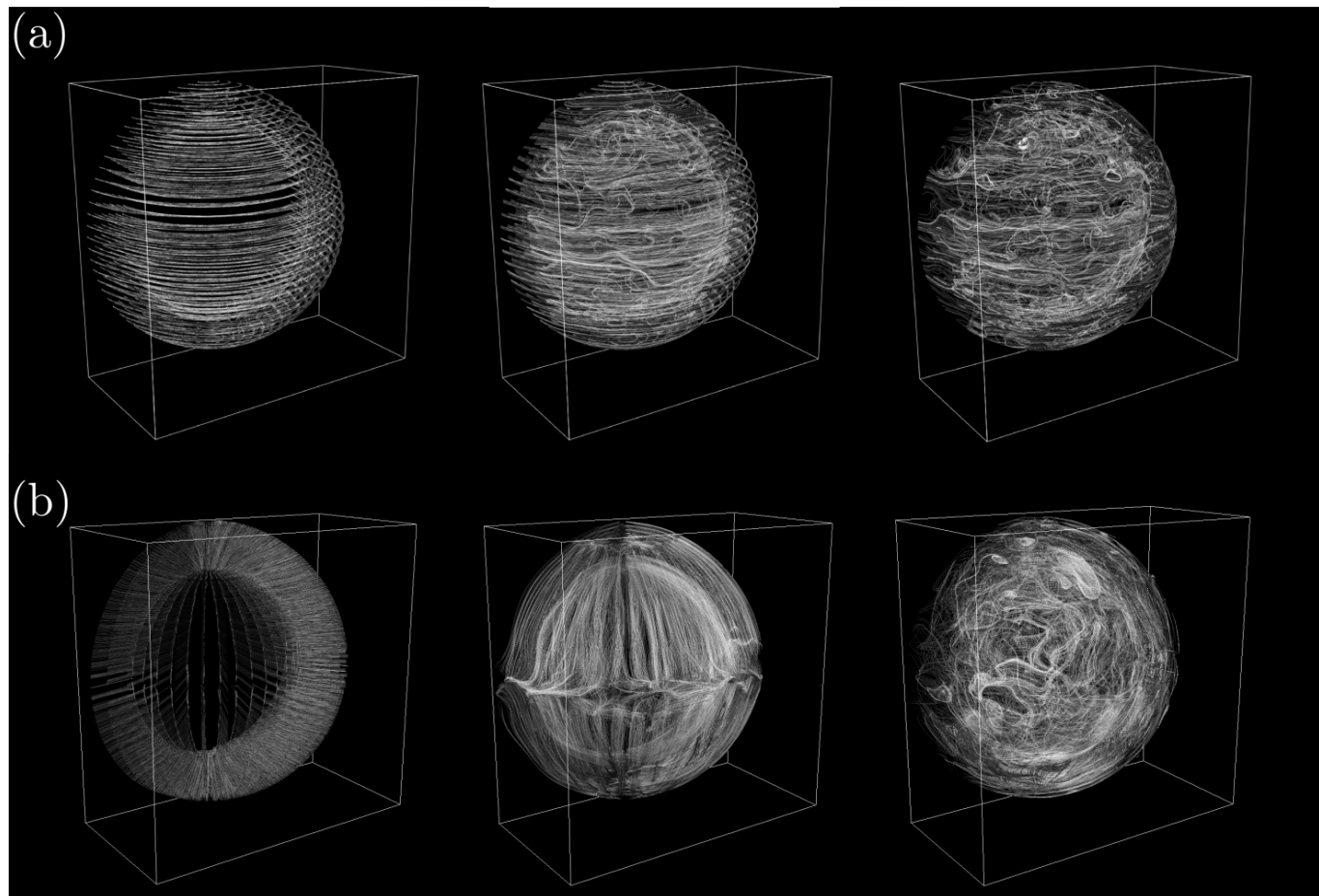


Fig. 13.— From left to right: Evolutions exhibiting Numerical evolution of (a) the magnetothermal instability (MTI) and (b) the heat flux driven buoyancy instability (HBI). Case (a) is initialized with a purely azimuthal field, and a temperature profile decreasing outwards, which is unstable to the MTI, and leads to an exponential growth in the radial component of the magnetic field. Case (b) starts with a purely radial field, and a temperature profile increasing outwards, which is unstable to the HBI, and leads to an exponential growth in the perpendicular component of the field. The free parameters of the EMHD theory are the same in both cases. Both cases use $128 \times 128 \times 128$ grid zones in $(R, \theta, \phi) \in [200M, 300M] \times (0, \pi) \times [0, \pi)$.

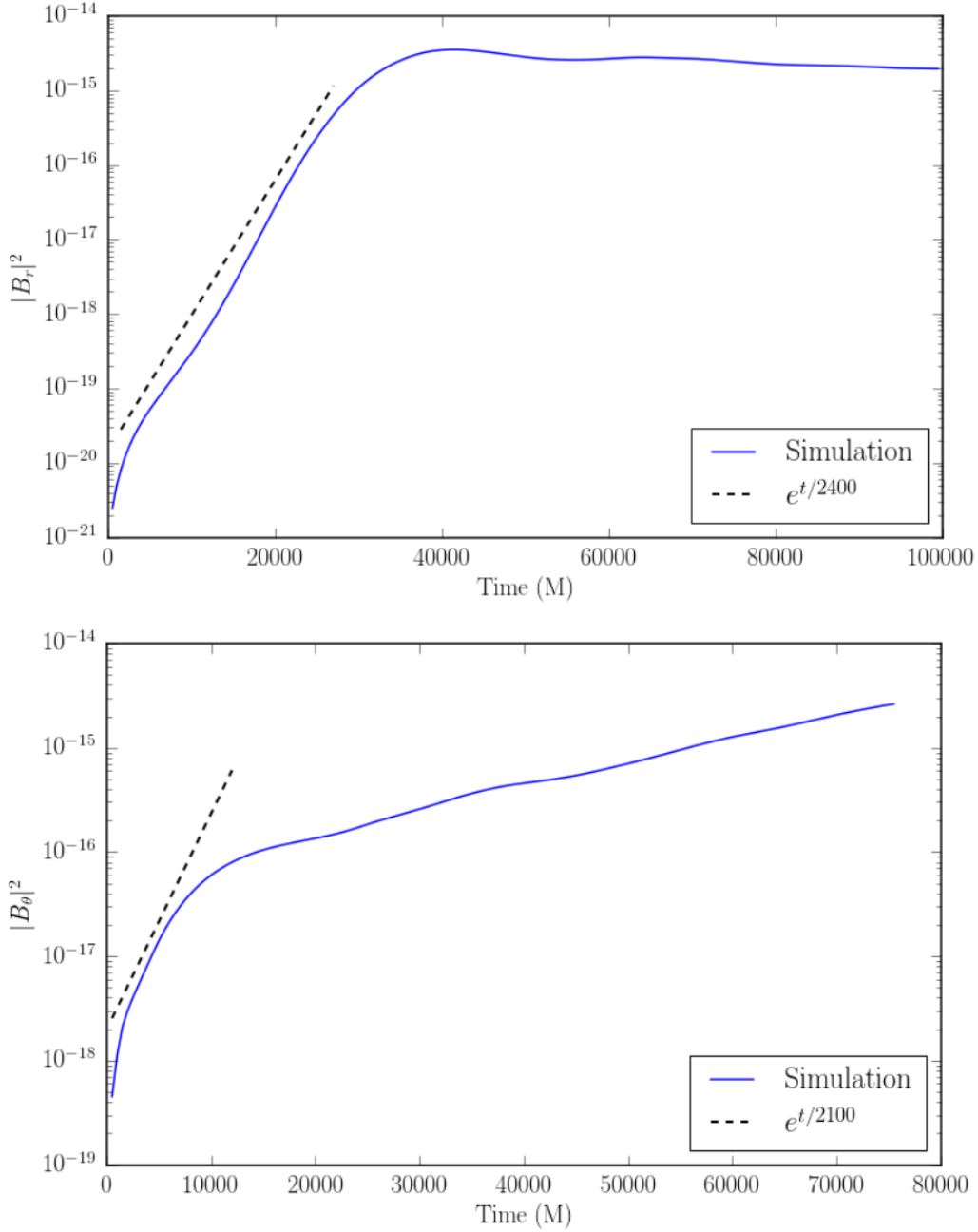


Fig. 14.— Top (bottom) panel : Growth of the radial (θ) component of the magnetic field in the 3D setup to study the MTI (HBI). The dotted line corresponds to an exponential growth with time scale ~ 2400 M (2100 M). In the limit where the conduction time scale is the fastest, as in our setups, the instabilities grow on a dynamical time scale, which for $R = 200$ M is ~ 2500 M (2000 M).

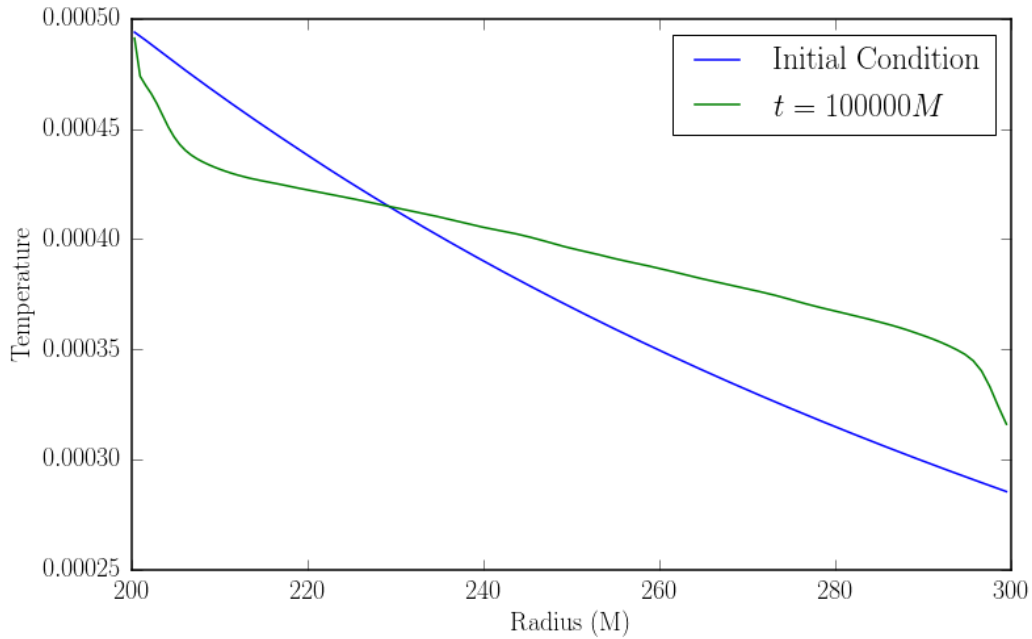


Fig. 15.— Initial and final radial temperature profiles (averaged over (θ, ϕ)) in the saturated state of the MTI. The instability is driven by the boundaries at $R = 200, 300$ M, which are held at fixed temperatures. The fixed temperature boundaries resist the flattening of the temperature profile due to the MTI, thus creating kinks in the temperature profile close to the radial boundaries.

9.1.2. Heat-Flux Driven Buoyancy Instability

The HBI requires magnetic field lines to be aligned with the temperature gradient for maximal growth, and so we seed the simulation with radial field lines $B^r = 10^{-3}/\sqrt{-g}$. The spatial domain is the same 3D half-sphere of the MTI setup. The boundary conditions, χ , and τ_R are also identical to the MTI case.

The initial conditions have $q = 0$, but $q_0 \sim \hat{b}^\mu(\nabla_\mu \Theta + \Theta a_\mu) \neq 0$. The heat flux q relaxes to q_0 over a timescale τ_R , leading to a finite radial heat flux. This heat flux feeds the HBI, which grows by kinking the field lines, and leads to an exponential growth of the radial component of the magnetic field. In the saturated state there is suppression of the heat flux below q_0 . Fig. 16 shows the intermediate state q_0 , which is unstable to the HBI, and the final saturated state.

9.2. Radiatively Inefficient Accretion Flow

The first astrophysical targets for the `grim` code are slowly accreting supermassive black holes. For a black hole with an accretion rate $\dot{M} \lesssim 0.01\dot{M}_{\text{Edd}}$ ($\dot{M}_{\text{Edd}} \equiv$ Eddington rate), we expect the surrounding accretion disk to be formed of a weakly collisional, magnetized plasma whose evolution is better approximated by our EMHD model than by the equations of ideal magnetohydrodynamics. We have already used the `grim` code to study the evolution of an accretion disk in the EMHD model in global, axisymmetric simulations. The current version of the `grim` code has also been tested on short preliminary evolutions of accretion disks in 3D, at low resolution.

In both cases, we find that the pressure anisotropy in the disk grows to values comparable to the magnetic pressure in the disk, reaching the mirror instability threshold. The closure used in our EMHD model then forces ΔP to saturate at $\approx b^2/2$. Longer, higher-resolution simulations are necessary to fully assess the impact of the EMHD model on the dynamics and energy budget of the system, and will be performed as sufficient computational resources become available.

Fig. 17 shows a snapshot of such a 3D evolution at $t = 1240GM/c^3$. The simulation was started from a hydrodynamical equilibrium torus Fishbone & Moncrief (1976) around a spinning black hole ($a = 0.9375$), seeded with a single loop of poloidal magnetic field. The initial amplitude of the plasma parameter $\beta \equiv 2P/b^2$ is ~ 100 in the inner disk, and $\beta \gtrsim 15$ everywhere. We see growth of magnetic turbulence due to the magnetorotational instability, and growth of the pressure anisotropy to the mirror instability threshold $\Delta P = b^2/2$. The heat flux is $\sim 10\%$ of its free-streaming value, a much larger effect than in earlier

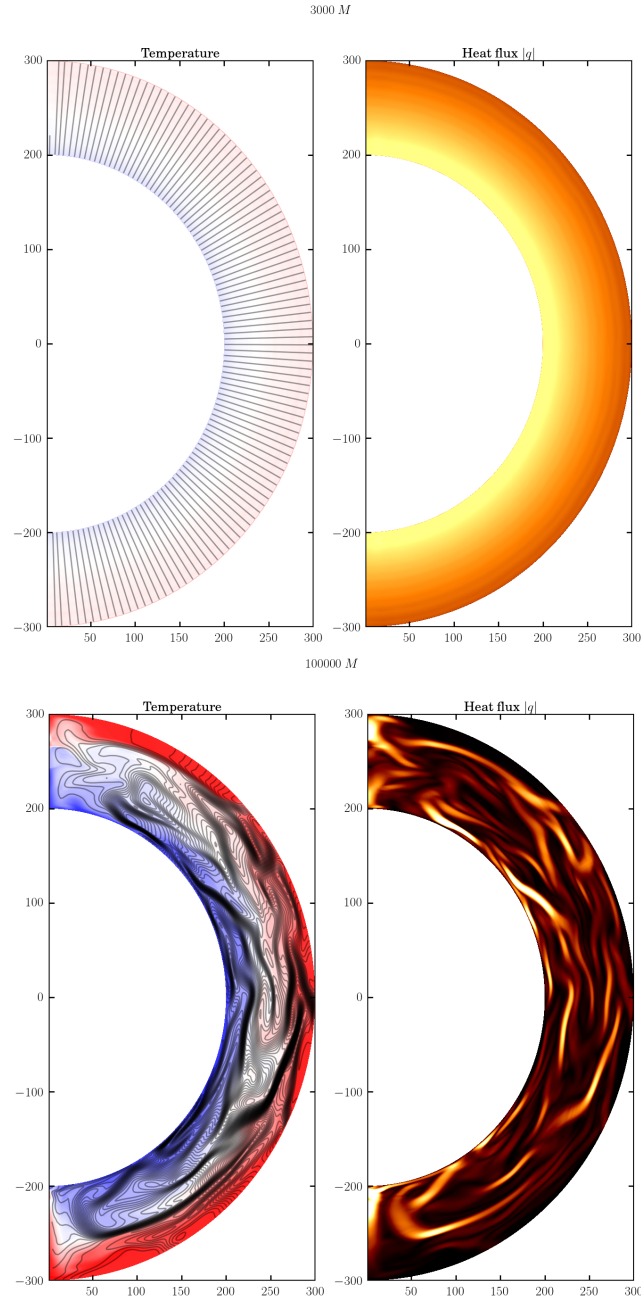


Fig. 16.— Above: The intermediate state of the HBI in a global 2D setup illustrating the finite radial heat flux that develops due to the presence of radial field lines connecting the constant temperature boundaries at $R = 200$ and $R = 300$ M. The initial conditions have zero heat flux, and are not shown here. Below: The saturated state of the HBI that suppresses the radial heat flux of the intermediate state.

axisymmetric simulations (Foucart et al. 2016).

10. Conclusion

Low luminosity black hole accretion flows ($L \ll L_{\text{edd}}$) are expected to be collisionless, so anisotropic dissipative effects can be important. Understanding the disk structure, and predicting observables requires the nonlinear solutions of relativistic dissipative theories in strongly curved space-times. Numerical codes so far can only evolve perfect fluids, with no heat conduction or viscosity. The algorithms developed for perfect fluids do not work for relativistic dissipative theories, because dissipation in the relativistic case is sourced by *spatio-temporal* gradients of the thermodynamic variables, as opposed to just spatial gradients in the non-relativistic case. In this paper, we have formulated and implemented a new scheme that can handle this situation and is physics-agnostic. We implement the scheme in a new code `grim`, which we then use to integrate the EMHD theory of anisotropic relativistic dissipation. The numerical solutions obtained have been checked against various analytic and semi-analytic solutions of the EMHD theory in both Minkowski and Schwarzschild space-times, in linear as well as in non-linear regimes.

The algorithm is the same as in Foucart et al. 2016 that has been used to study axisymmetric radiatively inefficient accretion flows, although here the code has been generalized to work in 3D, and now has the ability to run on either CPUs or GPUs. Thus we are able to make full use of the various node architectures in current and future generations of supercomputers. We use a performance model to show that the implementation is near-optimal, with the code achieving a significant fraction ($\sim 70 - 80\%$) of peak machine bandwidth. This, we show is crucial, because the performance of nonlinear solver that is at the heart of `grim` is primarily dependent on the machine bandwidth.

As example applications we have studied the magneto-thermal instability (MTI) and the heat flux driven buoyancy instability (HBI) in global 3D domains with a Schwarzschild metric, and evolved them to a nonlinear saturated state. Finally, we performed preliminary EMHD evolutions of a hydrodynamically stable torus in 3D, around a spinning (Kerr) black hole.

We thank Ben Ryan, Sasha Tchekhovskoy, Sean Ressler, Eliot Quataert, and Jim Stone for discussions as well as all the members of the horizon collaboration for their advice and encouragement (see `horizon.astro.illinois.edu`). The horizon collaboration is supported in part by NSF. We thank Pavan Yalamanchili at `ArrayFire` for his help with optimization. Support for this work was provided by NASA through an Einstein Postdoctoral Fellowship

grant numbered PF4-150122 awarded to FF by the Chandra X-ray Center, which is operated by the Smithsonian Astrophysical Observatory for NASA under contract NAS8-03060. MC was supported by an Illinois Distinguished Fellowship from the University of Illinois and by NSF grant AST-1333612. MC thanks Eliot Quataert for a Visiting Scholar appointment at the University of California, Berkeley, where part of this work was done. CFG was supported by NSF grant AST-1333612, a Simons Fellowship, and a visiting fellowship at All Souls College, Oxford. CFG is also grateful to Oxford Astrophysics for a Visiting Professorship appointment. This work was made possible by computing time granted by UCB on the Savio cluster.

REFERENCES

- Komissarov, S. S. 1999, *MNRAS*, 303, 343
- Beckwith, K., & Stone, J. M. 2011, *ApJS*, 193, 6
- Blandford, R. D., & Znajek, R. L. 1977, *MNRAS*, 179, 433
- Braginskii, S. I. 1965, *Reviews of Plasma Physics*, 1, 205
- Fishbone, L. G., & Moncrief, V. 1976, *ApJ*, 207, 962
- Chandra, M., Gammie, C. F., Foucart, F., & Quataert, E. 2015, *ApJ*, 810, 162
- Eckart, C. 1940 *Phys. Rev.* 58, 919 Tóth, G. 2000, *Journal of Computational Physics*, 161, 605
- Harten, A., Lax, P., & van Leer, B. 1983, *SIAM review.* 25(1):35-61
- Hiscock, W. A., & Lindblom, L. 1983, *Annals of Physics*, 151, 466
- Hiscock, W. A., & Lindblom, L. 1985, *Phys. Rev. D*, 31, 725
- Hiscock, W. A., & Lindblom, L. 1988, *Physics Letters A*, 131, 509
- Hiscock, W. A., & Lindblom, L. 1988, *Contemporary Mathematics*, 71, 181-220
- White, C. J., Stone, J. M., & Gammie, C. F. 2015, arXiv:1511.00943
- Foucart, F., Chandra, M., Gammie, C. F., & Quataert, E. 2016, *MNRAS*, 456, 1332
- Gammie, C. F., McKinney, J. C., & Tóth, G. 2003, *ApJ*, 589, 444

- Tóth, G. 2000, *Journal of Computational Physics*, 161, 605
- Israel, W., & Stewart, J. M. 1979, *Annals of Physics*, 118, 341
- Noble, S. C., Gammie, C. F., McKinney, J. C., & Del Zanna, L. 2006, *ApJ*, 641, 626
- Evans, C. R., & Hawley, J. F. 1988, *ApJ*, 332, 659
- Gardiner, T. A., & Stone, J. M. 2005, *Journal of Computational Physics*, 205, 509
- Mahadevan, R., Quataert, E. 1997, *ApJ*, 490, 605
- McKinney, J. C., Tchekhovskoy, A., & Blandford, R. D. 2012, *MNRAS*, 423, 3083
- McKinney, J. C., & Gammie, C. F. 2004, *ApJ*, 611, 977
- Sharma, P., Quataert, E., & Stone, J. M. 2008, *MNRAS*, 389, 1815
- Tchekhovskoy, A., Narayan, R., & McKinney, J. C. 2011, *MNRAS*, 418, L79
- Tchekhovskoy, A., & Nemmen, R. 2016, (in prep)
- Liu, X.-D., Osher, S., & Chan, T. 1994, *Journal of Computational Physics*, 115, 200
- Jiang, G.-S., & Shu, C.-W. 1996, *Journal of Computational Physics*, 126, 202
- Colella, P., & Woodward, P. R. 1984, *Journal of Computational Physics*, 54, 174
- Michel, F. C. 1972, *Ap&SS*, 15, 153
- Mościbrodzka, M., Gammie, C. F., Dolence, J. C., Shiokawa, H., & Leung, P. K. 2009, *ApJ*, 706, 497
- Toro, E. F., Spruce, M., & Speares, W. 1994, *Shock Waves*, 4, 25
- Yuan, F., & Narayan, R. 2014, *ARA&A*, 52, 529
- Balbus, S. A. 2000, *ApJ*, 534, 420
- Quataert, E. 2008, *ApJ*, 673, 758
- SageMath, the Sage Mathematics Software System (Version 7.3)*, The Sage Developers, 2016,
<http://www.sagemath.org>.

Balay, S., Abhyankar, S., Adams, M. F., Brown, J., Brune, P., Buschelman, K., Dalcin, L., Eijkhout, V., Gropp, W. D., Kaushik, D., Knepley, M. G., McInnes, L. C., Rupp, K., Smith, B. F., Zampini, S., Zhang, H., PETSc webpage: <http://www.mcs.anl.gov/petsc>

Yalamanchili, P., Arshad, U., Mohammed, Z., Garigipati, P., Entschew, P., Kloppenborg, B., Malcolm, J. & Melonakos, J. 2015, ArrayFire - A high performance software library for parallel computing with an easy-to-use API. Atlanta: AccelerEyes. Retrieved from <https://github.com/arrayfire/arrayfire>

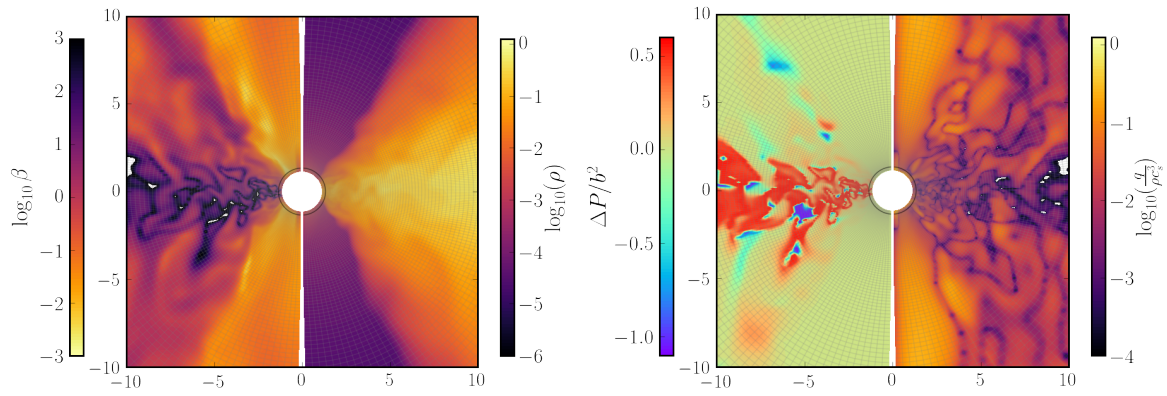


Fig. 17.— Vertical slice in the 3D evolution of a torus in the EMHD model, at time $t = 1240GM/c^3$. We show the plasma parameter $\beta = 2P/b^2$, density ρ , pressure anisotropy scaled to the magnetic energy $\Delta P/b^2$, and heat flux scale to the *free-streaming* heat flux $q/(\rho c_s^3)$.